Materials Today Bio 25 (2024) 100973

Contents lists available at ScienceDirect

Materials Today Bio

journal homepage: www.journals.elsevier.com/materials-today-bio

Photo-/thermo-responsive bioink for improved printability in extrusion-based bioprinting

Seo Hyung Moon [a], Tae Yoon Park [c], Hyung Joon Cha [c,d], Yun Jung Yang [a,b,*]

[a] Department of Biological Sciences and Bioengineering, Inha University, Incheon, 22212, Republic of Korea
[b] Inha University Hospital, Incheon, 22332, Republic of Korea
[c] Department of Chemical Engineering, Pohang University of Science and Technology, Pohang, 37673, Republic of Korea
[d] Medical Science and Engineering, School of Convergence Science and Technology, Pohang University of Science, Pohang, 37673, Republic of Korea

ARTICLE INFO

Keywords:
Silk fibroin
Iota-carrageenan
Bioink
Extrusion-based bioprinting
Dual-crosslinking

ABSTRACT

Extrusion-based bioprinting has demonstrated significant potential for manufacturing constructs, particularly for 3D cell culture. However, there is a greatly limited number of bioink candidates exploited with extrusion-based bioprinting, as they meet the opposing requirements for printability with indispensable rheological features and for biochemical functionality with desirable microenvironment. In this study, a blend of silk fibroin (SF) and iota-carrageenan (CG) was chosen as a cell-friendly printable material. The SF/CG ink exhibited suitable viscosity and shear-thinning properties, coupled with the rapid sol-gel transition of CG. By employing photo-crosslinking of SF, the printability with Pr value close to 1 and structural integrity of the 3D constructs were significantly improved within a matter of seconds. The printed constructs demonstrated a Young's modulus of approximately 250 kPa, making them suitable for keratinocyte and myoblast cell culture. Furthermore, the high cell adhesiveness and viability (maximum >98%) of the loaded cells underscored the considerable potential of this 3D culture scaffold applied for skin and muscle tissues, which can be easily manipulated using an extrusion-based bioprinter.

1. Introduction

Three-dimensional (3D) printing is a cutting-edge technology that enables the layer-by-layer creation of prototypes based on computer-aided design (CAD) models. This technique has found widespread adoption across various industries such as automotive, textile, food manufacturing, and medical applications, dating back to the 1980s [1,2]. In the field of medical applications, particularly in the early stages, inorganic materials, metals, and ceramics have been utilized for dental restorations and prosthetic supplies [3,4]. However, as the demand for scaffolds for both soft and rigid tissues has grown, synthetic polymers such as poly(ε-caprolactone) (PCL), poly(ethylene) glycol (PEG), poly lactic acid (PLA), and polyurethane (PU) have emerged as promising materials due to their adjustable mechanical properties, high structural integrity, and controllable degradability [5,6]. The use of organic 3D ink has enabled the creation of tunable topologies with high reproducibility, resulting in the precise replication of 3D microenvironments [7,8]. When the 3D printing technique is applied directly to biomaterials containing biomolecules and/or living cells (collectively referred to as bioink), it is more specifically referred to as 3D 'bio'printing [9,10].

In addition to cell embedding, achieving appropriate mechanical properties comparable to native skin is essential for scaffolds. The modulus of the material plays a critical role in regulating cell attachment and spreading [11]. By being able to adjust the mechanical properties of the scaffold more easily and accurately, it becomes possible to customize the cellular environment to match specific tissue requirements. Furthermore, aging and disease can lead to alterations in the mechanical integrity of the matrix composition, making the tunability of polymeric networks a highly significant requirement [12–14].

Among the various bioprinting techniques, extrusion-based printing, dispensing ink materials through the nozzle by physical force (e.g., piston or metal screw) and pneumatic pressure is one of the most extensively used modality. It is due to its cost-effectiveness, ability to fabricate human scale-tissue into millimeter size, multiple solidification methods, and wide range of biomaterials with high cell densities (e.g., $>1 \times 10^6$ cells/mL or even spheroids) [15–18]. Even if it has a lower printing resolution (>100 μm) than other methods (laser-based or inkjet printing), it has surmounted select the suitable ink materials which have appropriate rheological properties (i.e., enough viscosity, shear thinning properties, and yield stress) and rapid sol-gel transition [17–19]. Moreover, there is a greatly limited number of bioink candidates

* Corresponding author. Department of Biological Sciences and Bioengineering, Inha University, Incheon, 22212, Republic of Korea.
E-mail address: yj.yang@inha.ac.kr (Y.J. Yang).

https://doi.org/10.1016/j.mtbio.2024.100973
Received 12 July 2023; Received in revised form 18 January 2024; Accepted 22 January 2024
Available online 26 January 2024

Abbreviation

3D	Three-dimensional
CAD	Computer-aided design
CG	Carrageenan
ECM	Extracellular matrix
LVER	Linear viscoelastic region
PBS	Phosphate-buffered saline
PCL:	Poly(ε-caprolactone)
PEG	Poly(ethylene) glycol
PLA	Poly lactic acid
Pr	Printability index
PU	Polyurethane
Rubpy	Tris(2,2-bipyridyl) dichlororuthenium(II) hexahydrate
SEM	Scanning electron microscopy
SF	Silk fibroin
SPS	Sodium persulfate

exploited with extrusion-based bioprinting, as they meet the opposing requirements for printability with indispensable rheological features and for biochemical functionality with desirable microenvironment [8]. Less than 10% of synthetic polymers have been suitable for application in 3D artificial tissue/organ scaffolds, hindering direct printing with live cells due to their harsh printing conditions (use of toxic solvents and higher melting points and pressure), difficulty to encapsulate cells, lack of biological characteristics found in natural extracellular matrix (ECM) [12].

Natural polymers, including proteins and polysaccharides such as alginate, gelatin, collagen, silk, chitosan, and cellulose, offer a promising alternative in bioprinting due to their excellent biodegradability and ability to recruit cells on the ECM [20]. However, this paper addresses the existing limitations related to the inadequate printability of natural polymers and their low structural durability [11,20]. To overcome these challenges, dual-crosslinking strategies are proposed and discussed below, presenting a potential solution to these issues.

Light-activated photocrosslinking has gained significant attention as a promising method in bioprinting, primarily due to its non-invasive nature and the ability to achieve rapid gelation by forming chemical bonds within and between molecules. This technique offers convenient control over parameters such as light intensity, irradiation distance, and exposure time [21]. In this study, silk fibroin (SF), an FDA-approved natural protein derived from *bombyx mori*, was utilized as the 3D scaffold backbone, with tyrosines serving as the light-reactive moieties. A key advantage of this approach is that it eliminates the need for additional processes to introduce photo-activated functional residues (e.g., methacryloyl), thus avoiding any potential reduction in the bioactivity of pristine SF [13,22]. The rapid gelation process, completed within seconds, not only improves printability but also facilitates effective cell encapsulation by circumventing harsh printing conditions.

Furthermore, to address the issue of shrinkage, iota-carrageenan (CG), a negatively charged sulfonated polysaccharide extracted from red algae, was incorporated with SF [23]. The inclusion of CG not only helps overcome the problem of shrinkage but also enhances the thermo-responsive gelling capacity of the bioink through the ionotropic gelation mechanism. This results in notable changes in the rheological properties of the bioink, including the desirable shear-thinning behavior. Moreover, innate hydrophilicity, swellability and resemblance with native glycosaminoglycans of CG allows the 3D constructs with hydrated microenvironments and proper surface wettability, leading to enhance cell adhesion and proliferation [24].

In this study, the SF/CG bioink specifically designed for extrusion-based bioprinting, aiming to determine its effectiveness in reconciling conflicting requirements. The bioink exhibited superior printability with maintaining the necessary rheological properties. Also, its creates microenvironment conducive to desired cellular behavior. The fabricating complex 3D structures closely resemble native tissues, ensuring high shape fidelity. The ultimate goal of this evaluation was to assess the applicability of the SF/CG bioink in tissue regeneration applications.

2. Materials and methods

2.1. Silk fibroin (SF) extraction

The raw silk cocoons (*Bombyx mori,* Uljin silk farm, Korea) were cut into small pieces and degummed two times with 0.3 mM sodium oleate (Junsei, Japan) and 0.5 mM sodium carbonate (OCI, Korea) solution at 103°C for 40 min. Remnant salt was removed by boiling silk in distilled water twice at 100°C for 20 min [25,26]. The obtained silk fibroin (SF) was rinsed thoroughly with distilled water and dried in a fume hood at room temperature for two days. Dried SF was dissolved in a ternary solvent consisting of calcium chloride (Samchun, Korea), distilled water, and ethyl alcohol (Duksan, Korea) with the molar ratio of 1:8:2. The reaction was continued at 91°C for 3 h. The dialysis was performed with a cellulose membrane tube (MWCO: 12–14 kDa) against distilled water. The distilled water was exchanged seven times every 5 h for 3 days at room temperature. The clear supernatant was collected after centrifugation (9000 rpm for 10 min) and lyophilized (FD8508, IlShinBioBase, Korea). The SF powder was vacuum-packed for long-term preservation.

2.2. SF/CG bioink preparation

The SF and iota-carrageenan (CG) (Sigma Aldrich, USA) were dehydrated in the oven at 50°C for 10 min. Both were dissolved in PBS (pH 7.4) for 20% (w/w) SF and 1–3% (w/w) CG. The SF/CG bioink combinations are as follows: SF95CG5, SF91CG9 and SF87CG13 (sole silk for SF100). 1 mM Rubpy (Tris(2,2-bipyridyl) dichlororuthenium(II) hexahydrate), Sigma Aldrich, USA) and 50 mM sodium persulfate (SPS, Samchun, Korea) were added to the ink solutions. The ink solutions were incubated at 60°C for 3 min to completely dissolve the CG. After cooling to 37°C, HaCaT and C2C12 cells were incorporated into SF/CG ink solutions at 1×10^6 cells/ml to form cell-laden bioinks. SF/CG bioink were equilibrated at room temperature for 5 min before printing to achieve complete viscosity and rheological properties.

2.3. 3D printer parameter settings and optimization

The extrusion-based printer (INVIVO, Rokit, Korea) was redesigned for light-induced 3D printing. The LED light (420–480 nm, 2000–2500 mW/cm^2, T-king, USA) was equipped besides the nozzle, masked by black shield. The extruder setting temperature (25°C, 40°C, and 65°C), extrusion speed (1 mm/s, 3 mm/s, 5 mm/s, 7 mm/s) and nozzles gauge (23 G, 25 G and 27 G) were tested to have reproducible streaks. Computer-aided design (CAD) software (NewcreatorK, Rokit, Korea) and Image J (National Institutes of Health, Bethesda, MD, USA) were used for constructs design and image analysis, respectively.

To determine the optimal printing parameters, both spreading ratio [27] and printability index (Pr) [28] were evaluated using the following equations (1) and (2) respectively from the printed bioink with 0/90° pattern at varied parameters (ink formulation, extrusion speed, nozzle gauge and infill ratio), where L is the perimeter and A is the area of pore.

$$Spreading\ ratio = Printed\ needle\ diameter / Needle\ diameter \quad (1)$$

$$Pr = L^2 / 16A \quad (2)$$

Shape fidelity was calculated as below equation (3) [29], assuming that volumetric comparison between 3D virtual model and printed scaffolds could be extracted from dimensions in all directions (top, side, and front).

$$\text{Shape fidelity} = \left(Area_{printed}/Area_{virtual}\right)^{3/2} \quad (3)$$

2.4. Mechanical property analysis of SF/CG 3D construct

The SF/CG bioink was photo-crosslinked in Teflon mold (20 mm × 5 mm) and was irradiated 450 nm blue ray for 30 s. The gel was immersed in distilled water for 1 h for swollen equilibrium networks. The tensile properties of hydrogels were carried out with a universal testing machine (34SC-1, INSTRON, USA). The operation distance between grips was 10 mm and crosshead speed was set by 5 mm/min. The thickness of hydrogels was measured using a digimatic micrometer (MDC-25SX, Mitutoyo Corporation, Japan). Tensile stress (kPa), strain (mm/mm) and stiffness modulus (kPa) were derived from the stress-strain curves obtained by the tensile test.

2.5. Scanning electron microscopy (SEM)

The 3D constructs were sputter-coated (Turbo Pumped Sputter Coater Q 150T, Quorum, UK) with platinum at 20 mA for 120 s. The image was acquired by scanning electron microscopy (SEM, S-4300SE, HITACHI, Korea) with an accelerating voltage of 15 kV and 300 × magnificent. 50 pores in each sample were selected randomly and microscopic pore size was calculated with Image J.

2.6. Swelling ratio calculation

The SF and SF/CG hydrogels (m_{iw}) were freeze-dried (m_{id}) and incubated in PBS (pH 7.4) at 37°C for a day. The swollen hydrogels (m_s) were freeze-dried (m_d) again, and weights of hydrogels in each step (m_{iw}, m_{id}, m_s, m_d) were recorded. The swelling ratio (q) were calculated as follows (4) [30].

$$\text{Swelling ratio q} = m_s/m_d \quad (4)$$

2.7. Contact angle measurement

Water drop contact angles were examined by using a contact angle goniometer (Phoenix 300 touch, Surface Electro Optics Co., Korea) equipped with Surfaceware 9 (Surface Electro Optics Co., Korea). 10 μl water droplet was deposited onto flat surface of SF100, SF95CG5, SF91CG9 and SF87CG13 constructs. The contact angle was estimated by using image J.

2.8. Rheological property analysis of SF/CG 3D bioink

To analyze the dynamic viscoelasticity of the bioink varying ratio of SF/CG (SF100, SF95CG5, SF91CG9 and SF87CG13), oscillatory measurements were performed using a rheometer (DHR-1, TA instruments, USA) with cone-shape (2°, 20 mm diameter) geometry and a gap of 58 μm. The linear viscoelastic region (LVER) and yield strain were determined by strain sweep tests ranging from 0.1% to 100 % strain at an oscillation frequency of 1 rad/s. The viscoelastic values of modulus (G′, G″) were obtained from frequency sweep tests ranging from 0.1 rad/s to 100 rad/s at 1% strain.

2.9. Viscosity measurement of SF/CG bioink

SF95CG5, SF91CG9, and SF87CG13 bioinks were incubated at 60°C with agitation for 5 min. The samples were then cooled to 25°C and placed in a viscometer (DV2TRVCP, Brookfield, USA), equipped with a cone-shape spindle (CPA-52Z, Brookfield, USA). The shear stress and viscosity of each SF95CG5, SF91CG9, and SF87CG13 bioink were measured under different rotation speeds ranging from 0.2 s^{-1}–100 s^{-1}. The measurements were obtained for 30 s at 25°C and 40°C, respectively, for 30 s, and each measurement was replicated three times.

2.10. Cell proliferation and viability test

The 1 × 10^3 human keratinocyte HaCaT and mouse myoblast C2C12 cells (kindly provided by K.J. Kim at Inha University, Korea) were attached to the cylindrical-shaped SF/CG hydrogel (7 mm diameter × 2 mm height) at 37°C in 5% CO_2 incubator. The HaCaT cells were cultured with Dulbecco's Modified Eagle's Medium/high glucose (DMEM, Gibco, USA) supplemented with 10% (v/v) fetal bovine serum (FBS, Gibco, USA) and penicillin/streptomycin (HyClone, USA). The cell proliferation was determined using Cell Counting Kit-8 (CCK-8, Dojindo, Japan), followed by the manufacturer's instructions. The absorbance at 450 nm was measured using a microplate absorbance spectrophotometer (EPOCH2, BioTek, Korea).

Cell viability in the 3D cell-laden constructs was investigated using LIVE/DEAD™ Viability/Cytotoxicity kit (Invitrogen, USA) according to the manufacturer's protocol. In brief, the 1 × 10^6 HaCaT and C2C12 cell-laden bioinks (SF100 and SF91CG9) were extruded as droplets in 96 well plates. Those were also printed as multi-layer lattice with 10 × 10 mm dimension). All these cell-laden constructs were photo-crosslinked for 30-sec irradiation, followed by SPS/Rubpy removal (washing for 5 min, three times). After incubation, scaffolds at day 3 were rinsed and stained with 1 μM Calcein AM and 2 μM ethidium homodimer-1 (EthD-1) diluted in DPBS (Gibco, USA) for 40 min (37°C, 5% CO_2). The digital imaging system (CELENA S, Logos Biosystems, Korea) were used for z-stack fluorescence images. From the obtained images, cell viability was calculated using Image J as follows (5) [31,32].

$$\text{Cell viability } (\%) = [Live\ cells\ /\ (Live\ cells + Dead\ cells)] \times 100 \quad (5)$$

2.11. Degradation test

The SF/CG bioink (7 mm × 2.4 mm) was crosslinked in a cylinder plastic mold for 30-sec irradiation. The cylinder constructs placed in 24 well plates with pH 7.4 PBS containing with or without 0.001 units/ml of protease XIV (*Streptomyces griseus*, Sigma Aldrich). The immersed samples were taken out at predetermined time intervals, wiped superficially with kimwipes, weighed, and placed again in the well with fresh solution. The solution was replaced every two days after measurements.

Weight loss was calculated using the equation (6) [33]. The experiment was conducted triplicated (n =3) under identical conditions.

$$\text{Weight loss } (\%) = [(W_0 - W_1)\ /\ W_0]x\ 100 \quad (6)$$

W_0: initial weight of the hydrogel.

W_1: final weight of the hydrogel each interval.

2.12. Carbohydrate (CG) quantification

The phenol-sulfuric acid assay was performed to quantify released carrageenan from SF/CG 3D constructs. A SF/CG 3D constructs (cylinder type, 10 mm × 3 mm) were immersed in PBS and incubated at 60°C and 37°C for 5 weeks, respectively. The released SF and CG were collected every 3 days, and replaced by PBS. The absorbance of each solution was measured at 490 nm and compared with a D-(+)-glucose (Dextrose, MB Cell, Korea) standard curve.

2.13. Fourier transform infrared spectroscopy analysis

The intermolecular interaction of SF/CG constructs was analyzed using the FT-IR (VERTEX 80V, Bruker). Performed samples (SF100, SF95CG5, SF91CG9, SF87CG13, and CG100) were combined with KBr, then pressed into disc molds to be prepared for the analysis. The absorption spectra were recorded by 64 scans with a resolution of 4 cm^{-1} within the wavenumber range of 400 cm^{-1} and 4000 cm^{-1}.

2.14. Statistical analysis

Statistical significance was analyzed by paired Student's t-test using SigmaPlot Software (Systat Software Inc., USA). Differences with p-values of less than 0.05 were considered statistically significant (*: P <0.05, **: P <0.01, ***: P <0.001).

3. Results and discussions

3.1. Photo-crosslinkable and temperature-responsible SF/CG bioink

The natural fibrous protein silk fibroin (SF) is highly valued in bioscaffold applications due to its robust mechanical properties attributed to its crystalline beta-sheet structure [34]. However, the solubilization of high molecular weight SF has been challenging as it typically requires acidic or alkaline solvents, limiting its compatibility with cell encapsulation [35,36]. To address this, we enzymatically cleaved SF into smaller fragments ranging from 45 to 100 kDa, enabling its solubilization in ambient temperature and pH conditions, such as phosphate-buffered saline (PBS). The resulting PBS-soluble silk offers a distinct advantage for encapsulating various biological factors or mammalian cells while maintaining high cell viability under mild printing conditions [37]. However, utilizing solely SF as a protein-based ink for cell encapsulation presents certain limitations, such as aggregation-induced clogging of printing nozzles during extrusion and shrinkage issues in 3D structural constructs due to its low viscosity and inadequate rheological properties [16,38]. Here, dual-crosslinking strategy attempted to meet the requirements in printability and physical/mechanical/biological properties for 3D printed construct (Fig. 1).

To enable the use of PBS-soluble silk ink in extrusion-based 3D printing, two crosslinking strategies were considered. The first strategy involved tyrosine-tyrosine photo-crosslinking, a widely utilized method in tyrosine-rich native proteins that require robust mechanical characteristics, such as resilin in fleas or wing tendons from adult dragonflies [39]. The tyrosine occupies 4.98 mol% of whole amino acids in silk, which was sufficient to provoke gelation within a few seconds [40,41]. This dityrosine-based photo-crosslinking approach offers several advantages, including the avoidance of UV-induced genetic damage to encapsulated cells, rapid gelation in just a few seconds at low initiator concentrations, and the ability to penetrate deep tissue layers (around 250 μm up to 2 mm deep tissue) with visible light (400–450 nm) activation [42,43]. Furthermore, this visible light-activated crosslinking system enables the efficient stacking of laminated protein solutions in the extrusion-based printer, ensuring the structural integrity of self-standing 3D constructs with excellent resolution [44–47].

The second crosslinking strategy involved temperature-assisted physical crosslinking. Unlike other 3D printing methods, extrusion-based printing requires shear-thinning properties and a minimum viscosity of 30 mPa s for the ink [48]. To achieve this, iota-carrageenan (CG) was incorporated as a viscosity enhancer and temperature-responsive material. CG undergoes a reversible transition from an ordered helix conformation to a disordered random coil conformation at around 60°C [49]. This sol-gel transition of CG allowed for increased viscosity in SF/CG blends, resulting in improved printing accuracy with reduced initial filament diffusion. Additionally, it endowed the bioink with desirable rheological properties, such as shear-thinning behavior, relieving the stress on encapsulated cells during extrusion in response to shear forces at the nozzle orifice (Fig. S1) [50]. Furthermore, the incorporation of CG facilitated the homogeneous distribution of cells in self-standing layers, ensuring good fidelity in the printed constructs [48,51].

3.2. Mechanical properties of 3D constructs

The physical characteristics of a 3D construct, such as surface charge/wettability, swellability, pore size, and inter-porosity, play a crucial role in governing cell interactions within scaffolds. These characteristics have significant implications for cell-specific migration, initial adhesion, morphology, and the diffusion coefficient of bioactive molecules, including nutrients, growth factors, and cell-secreted wastes [52–54]. The physical properties of a 3D construct are strongly influenced by the network density, which can be enhanced by employing longer polymer chains (higher molecular weight) or generating a higher number of crosslink junctions, leading to a denser material structure [55].

As depicted in Fig. 2A, the SF87CG13 construct exhibited approximately 1.8-fold higher water absorption compared to SF alone. The degree of swelling varied among the different groups as the amount of CG increased. This suggests that while covalent crosslinks occur exclusively with SF, the physically attached CG enhances the expansion of the network through its water-absorption properties.

The surface hydrophilicity of 3D constructs, plays a significant role in promoting cell adhesion and growth [56,57]. The wettability of hydrogel surfaces influences the cell types, conformation, and binding interactions of proteins absorbed from the culture media, which further impact cell attachment [58]. For instance, fibroblast adhesion is maximized on surfaces with a contact angle ranging from 60° to 80° [58,59]. In the case of our constructs, SF87CG13, SF91CG9, and SF95CG5 exhibited contact angles of 64.6° ± 1.4°, 69.1° ± 1.0° and 75.5° ± 1.7° (Fig. 2B). In contrast, SF100 was relatively hydrophobic with a contact

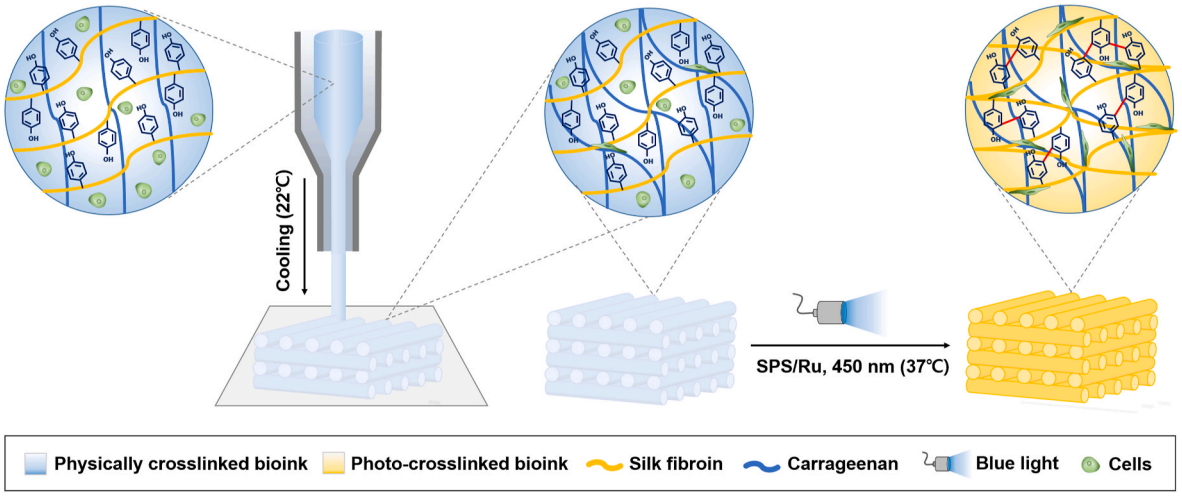

Fig. 1. Schematic of the printing process of SF/CG bioink.

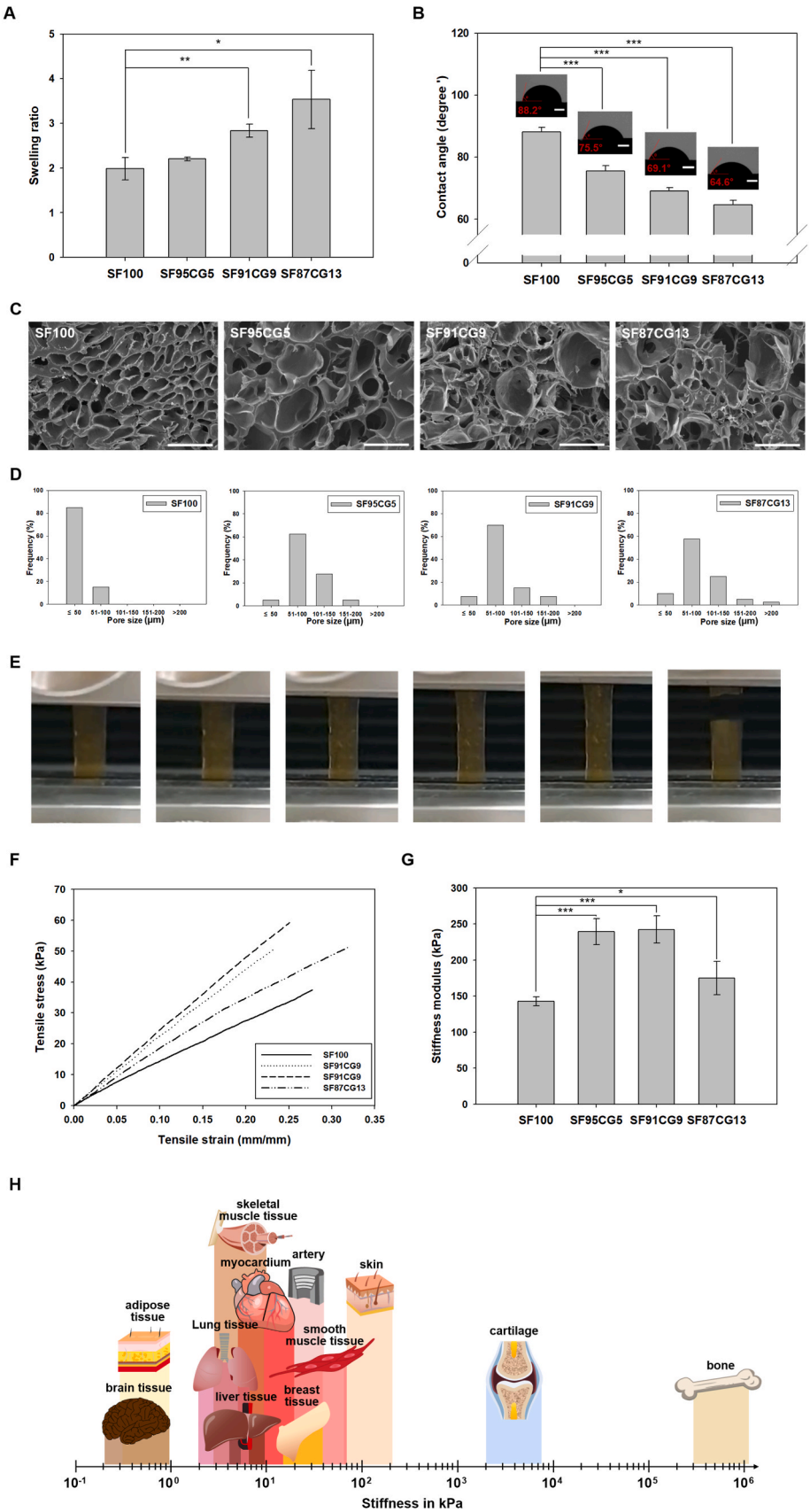

Fig. 2. Physical properties of SF/CG constructs. (A) Swelling ratio and (B) contact angle measurement of 3D construct surface. (C) Scanning electron microscopy (SEM) images of cross-section and (D) the pore size distribution. (E) Photographs of tensile test process, (F) tensile stress-strain curves and (G) stiffness modulus of 3D constructs (SF100, SF95CG5, SF91CG9 and SF87CG13). (H) Schematic representation of stiffness modulus of different human tissues [74]. All error bars represent the standard deviations (n =7) with statistical significance (*p <0.05, **p <0.01, and ***p <0.005). Scale bars indicate 1 mm in (B) and 100 μm in (C).

angle value of 88.2° ± 1.4°. This can be attributed to the presence of two sulfate groups per repeating unit (two galactose molecules) in iota-carrageenan (iota-CG), which provide a more hydrophilic surface to the 3D constructs [60]. These findings demonstrate that iota-CG serves as a suitable material to enhance the surface hydrophilicity of the constructs, thus improving cell adhesion.

The pore size and its distribution within hydrogels significantly influence the viability of encapsulated cells [61]. Optimal pore sizes have been reported for various applications, including neovascularization (5 μm), fibroblast ingrowth (5–15 μm), hepatocytes ingrowth (20 μm), adult mammalian skin (20–125 μm), osteoblast regeneration for mineralized bone (100–200 μm), osteoid ingrowth (40–100 μm), and rapid vascularization (500 μm) [62,63]. Specifically, for tissue development, a pore size range of 90–110 μm is considered adequate to support angiogenesis and the growth of new blood vessels, ensuring the supply of nutrients and oxygen. Pore sizes of 20–125 μm pores are necessary to facilitate migration of dermal and epidermal cells for skin regeneration [52,64,65]. Fig. 2C and D show the pore size distribution of various SF/CG constructs. The pore size distribution of pure SF is primarily below 50 μm, while the SF/CG constructs exhibit larger pore sizes in the range of 51–150 μm, with maximum pore sizes extending beyond 151–200 μm. The median pore size diameters, as measured by Image J, were as follows: 32.1 μm (SF100), 83.2 μm (SF95CG5), 77.9 μm (SF91CG9), and 79.3 μm (SF87CG13). Hence, the addition of CG resulted in an increase in the average pore size of the scaffold, aligning with the required pore sizes for mammalian skin cells.

The scaffold used for cellular applications must possess sufficient structural integrity to withstand the repetitive mechanical forces experienced within the body [66]. As a robust and implantable scaffold, it needs to exhibit adequate strength, stiffness (commonly referred to as Young's modulus), and toughness to prevent cracking until the seeded cells successfully replace the defects [67]. Additionally, each tissue type has its own specific Young's modulus requirements that an artificial scaffold should meet to ensure appropriate cell function, morphology, attachment, proliferation, and differentiation [67–74].

To assess the mechanical properties (strength, Young's modulus, and toughness), a tensile test was conducted and the stress-strain plot was derived (Fig. 2E) [75]. The tensile strength and strain were determined from the fracture point, while the Young's modulus was obtained from the initial linear slope of the stress-strain plot. The area under the curve before rupture represents the toughness of the material, indicating the amount of energy required for rupture [76].

According to Fig. 2F, and Table 1, the addition of CG to the 3D ink improved the tensile strength of the constructs. Specifically, SF91CG9 demonstrated a tensile strength increase of up to 160% (64.03 ± 6.25 kPa), SF95CG5 exhibited an increase of 137 % (54.67 ± 5.25 kPa), and SF87CG13 showed an increase of 130 % (51.82 ± 3.94 kPa) compared to pure silk (SF100, 40.01 ± 1.44 kPa). This enhancement can be attributed to the presence of CG in the hydrogel, which independently generates a cationic-induced double helix 3D network in addition to the covalently crosslinked network with SF [77]. No new adsorption peak appeared in the FTIR spectra of SF/CG blended structures besides the characteristic peaks corresponding to CG100 and SF, demonstrating no new chemical crosslinking formed between SF and CF (Fig. S2) [78]. The dual-crosslinking effect is maximized when the CG concentration is below 2% (w/v) in the ink. Ink formulations containing CG concentrations exceeding 3% (w/v) become excessively viscous, leading to poor blending and hindering the formation of a well-induced dityrosine crosslinking within SF. SF87CG13 presented the remarkable peak in the region of para-disubstituted benzenes (800-860 cm^{-1}), whereas no clear peak in the spectra of the SF100 constructs, which verified the complete crosslinking of tyrosines (Fig. S2) [41]. The mechanical strength of physically and chemically dual-crosslinked (PCDC) hydrogels depends not only on the inherent characteristics of the composition (in this case, SF/CG) but also on the effective distribution of the reinforcement (CG) within the network [79,80]. It is hypothesized that an optimal ratio exists for exerting the maximum stress, allowing a segment of CG to become entangled within the crosslinked network of SF, resulting in PCDC SF/CG structure with synergistic strength [81]. There were negligible differences in strain (82–107 %) across the constructs, indicating a positive correlation between the modulus and strength of the constructs with the proportion of CG. The relatively rigid SF95CG5 and SF91CG9 constructs exhibited increased stiffness modulus and decreased resilience compared to SF100 [82]. The stiffness modulus of the constructs defines whether the material is soft (compliant) or hard (rigid) based on its resistance to deformation under applied force [68].

Table 1
Mechanical properties of SF/CG constructs (SF100, SF95CG5, SF91CG9 and SF87CG13).

	Tensile strain (mm/mm)	Tensile strength (kPa)	Stiffness modulus (kPa)
SF100	0.28 (±0.02)	40.01 (±1.44)	142.8 (±6.2)
SF95CG5	0.23 (±0.01)	54.67 (±5.25)	239.57 (±18.19)
SF91CG9	0.26 (±0.02)	64.03 (±6.25)	242.57 (±18.95)
SF87CG13	0.3 (±0.02)	51.82 (±3.94)	175.15 (±23.24)

The stiffness modulus of the SF/CG 3D constructs was evaluated in comparison to real tissues. The modulus of the SF/CG constructs ranged from 175.15 ± 23.24 kPa to 242.57 ± 18.95 kPa (Fig. 2G). This range is consistent with the modulus of human skin tissue, particularly the dermis layer, which has an average modulus of approximately 200 kPa (Fig. 2H) [74,83,84]. Similarly, HaCaT cells on the 214 kPa-modulus polyacrylamide (PA) hydrogel presented improved spreading ability and cell interconnection compared to the soft 8 kPa gels [85]. Similarly, HaCaT cells cultured on polydimethyl siloxane (PDMS) matrices with a modulus of 375 kPa demonstrated increased spreading dynamics and proliferation compared to matrices with lower stiffness (50 kPa) [86]. The SF/CG constructs also exhibited comparable rigidity to other biological substrates such as skeletal muscle (~170 kPa), cornea (200 kPa), and the keratinocyte matrix (~340 kPa) [66,87,88].

3.3. Rheological and viscoelastic properties of the SF/CG bioinks

Shear thinning, or pseudoplasticity, is a notable non-Newtonian fluid behavior that manifests as a decrease in viscosity with increasing shear rate [89–91]. The shear-thinning properties of the bioink play a crucial role in achieving high printing pattern fidelity and maintaining the viability of suspended cells in extrusion-based printing processes [92]. This property enables smooth ink flow without nozzle clogging and promotes the retention of solid-like properties after extrusion onto the printing bed [93–96]. During extrusion, the bioink undergoes stress through a small orifice, necessitating mild shear to prevent adverse effects on the viability of suspended cells [97]. Shear thinning properties effectively reduce shear stress, mitigating the risk of cell death caused by cell membrane rupture [15,98].

Silk fibroin solution showed Newtonian fluids in case of low viscosity [97]. To induce shear thinning behavior and enhance viscosity, CG is introduced as a partner material in the SF/CG blend. This addition, particularly when combined with temperature-dependent gelation (Figs. S3A–B), promotes the formation of tightly aggregated double helix structures and reduces electrostatic repulsion between sulfate groups in the presence of cationic ions [99,100]. Notably, CG exhibits higher viscosity at 25°C compared to 40°C under the same shear rate (Fig. S4A). Increasing the shear rate leads to a decrease in both viscosity and shear stress, indicating the shear-thinning property that enables plug-like flow of the bioink [97,101,102]. Furthermore, the shear stress of SF95CG5 approaches zero at low shear rates (Fig. S4B), suggesting the presence of limited yield stress in the bioink [103]. The SF/CG blended bioink exhibits higher yield stress values and stronger shear thinning properties than the CG control. These characteristics, attributed to the sol-gel transition and resultant shear thinning properties of CG, are expected

to facilitate continuous bioink extrusion while maintaining shape integrity, improving fidelity of 3D constructs, and ensuring cell viability [104].

Viscosity plays a critical role in printability and shape fidelity [105]. SF alone has low viscosity (around 0.05–0.1 Pa s), making it challenging to achieve high printability without additional measures such as using higher molecular weight SF or incorporating additives for crosslinking during printing [106,107]. Thus, printing SF solution without additives is highly challenging [106,108–110]. Fig. 3A and B demonstrate a positive correlation between SF/CG viscosity and the ratio of CG, indicating the thickening role of CG in the bioink. The viscosity of SF/CG bioink, as measured by a viscometer, is approximately 3×10^5 mPa s, which falls within the suitable range for extrusion-based printing (between 30 and 6×10^7 mPa s) [48].

Rheological studies were performed to determine the behavior of the bioink as either a solid-like gel or a viscoelastic liquid [97]. The results of oscillatory strain sweep exhibited the viscoelastic behavior of all SF/CG inks (SF95CG5, SF91CG9, and SF87CG13), as confirmed by a linear viscoelastic region (LVER) of constant moduli with G' >G" (gel-like behavior) at low and medium strains, followed by transition to G" >G' at high strains (Fig. 3C) [111]. An oscillatory amplitude sweep at 1% strain, identified within the LVER, was conducted [112]. As shown in Fig. 3D, SF95CG5 exhibited both gel-like behavior and viscoelastic liquid behavior, depending on the frequency. At higher frequencies (>60 rad/s), the gel structure of SF95CG5 deformed, leading to a decrease in the storage modulus (G′). However, the crossover point was shifted to the right in SF91CG9 and SF87CG13 compared to SF95CG5. SF91CG9 and SF87CG13 demonstrated gel-like behavior, where the storage modulus (G′) dominated over the loss modulus (G″). Both G′ and G″ of the bioinks (SF91CG9, SF87CG13) increased with increasing frequency, indicating frequency dependency [97]. Overall, SF91CG9 and SF87CG13 acted as elastic gels. Elastic gel-like bioinks exhibited better shape fidelity in printed constructs but relatively lower cell viability compared to viscoelastic liquids [113]. To achieve 3D printing with high shape fidelity using extrusion-based techniques, the ink material should be extruded with high resolution and stop exiting the orifice immediately, which is not achievable with viscoelastic solutions [97].

3.4. 3D printed SF/CG constructs

To establish optimized printing parameters for high printing resolution and reproducibility, the printability was confirmed by varying diverse printing conditions, such as the ink composition (SF95CG5, SF91CG9, and SF87CG13), nozzle diameters (0.2 mm, 0.25 mm and 0.33 mm), and printing speeds (1 mm/s, 3 mm/s, 5 mm/s and 7 mm/s). The printed strand width was mechanically controllable by increasing printing speed with smaller nozzle diameter. By modifying formulation of bioinks, higher viscosity allow the precise strand to be printed and lower spreading ratio measured by dividing printed strand width by the nozzle inner diameter [27]. To set the optimal temperature of extruder, nozzle size and printing speed to print with high precision, optimal conditions were different according to each ink formulation verified with minimum spreading ratio (Fig. 4A–C, Fig. S5A, and Table S1). In addition, irradiation time was controlled varied by printing speed, allowing 2 s per line for extruding 5 mm to prevent pre-gelation owing to insufficient crosslinking time or shrinking and nozzle clogging issues

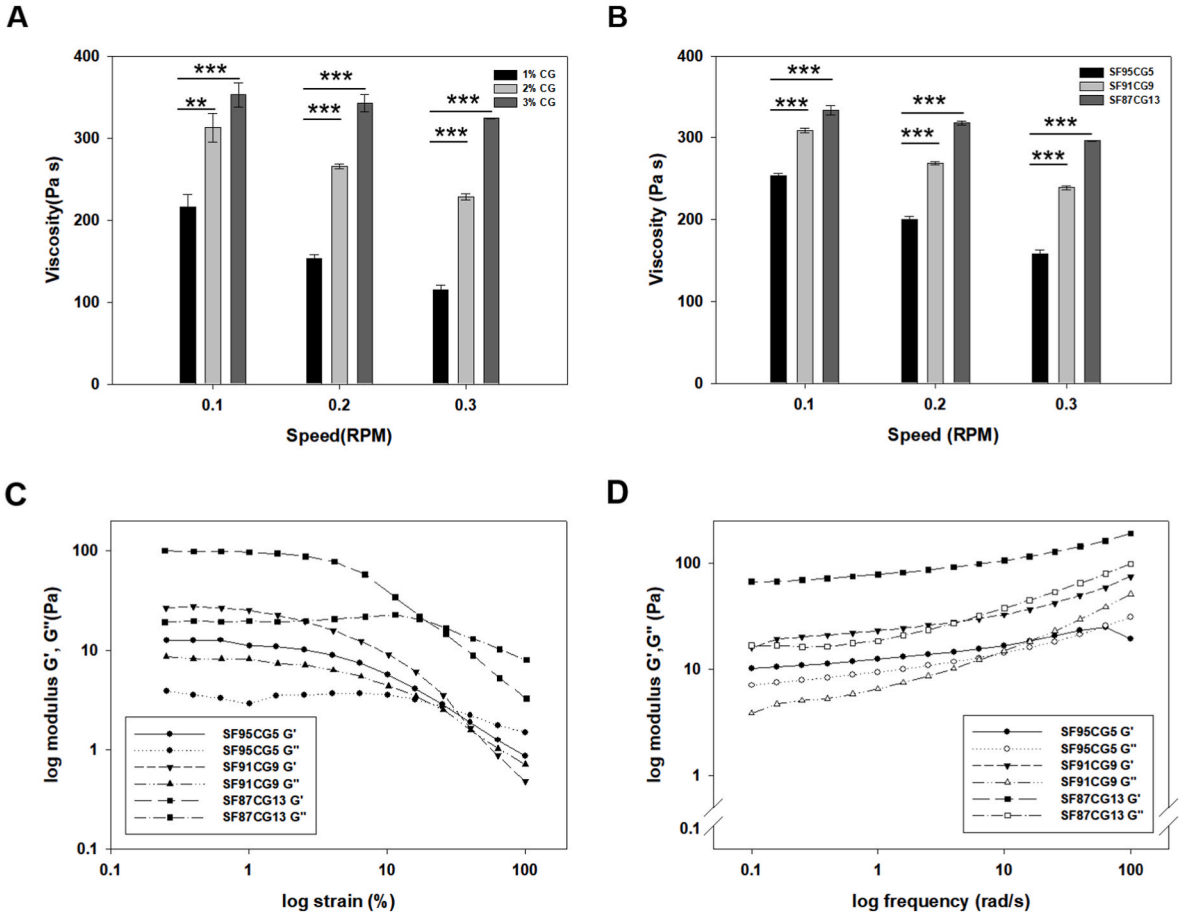

Fig. 3. Evaluation of the viscoelastic properties of the SF/CG bioink. (A) Viscosity as a function of shear rate for iota carrageenan solutions (1%, 2% and 3% (w/v)) and (B) bioink (SF95CG5, SF91CG9 and SF87CG13). Oscillatory rheological measurement performed under (C) strain sweep and (D) frequency sweep. All error bars represent the standard deviations (n =3) with statistical significance (**p <0.01, and ***p <0.005).

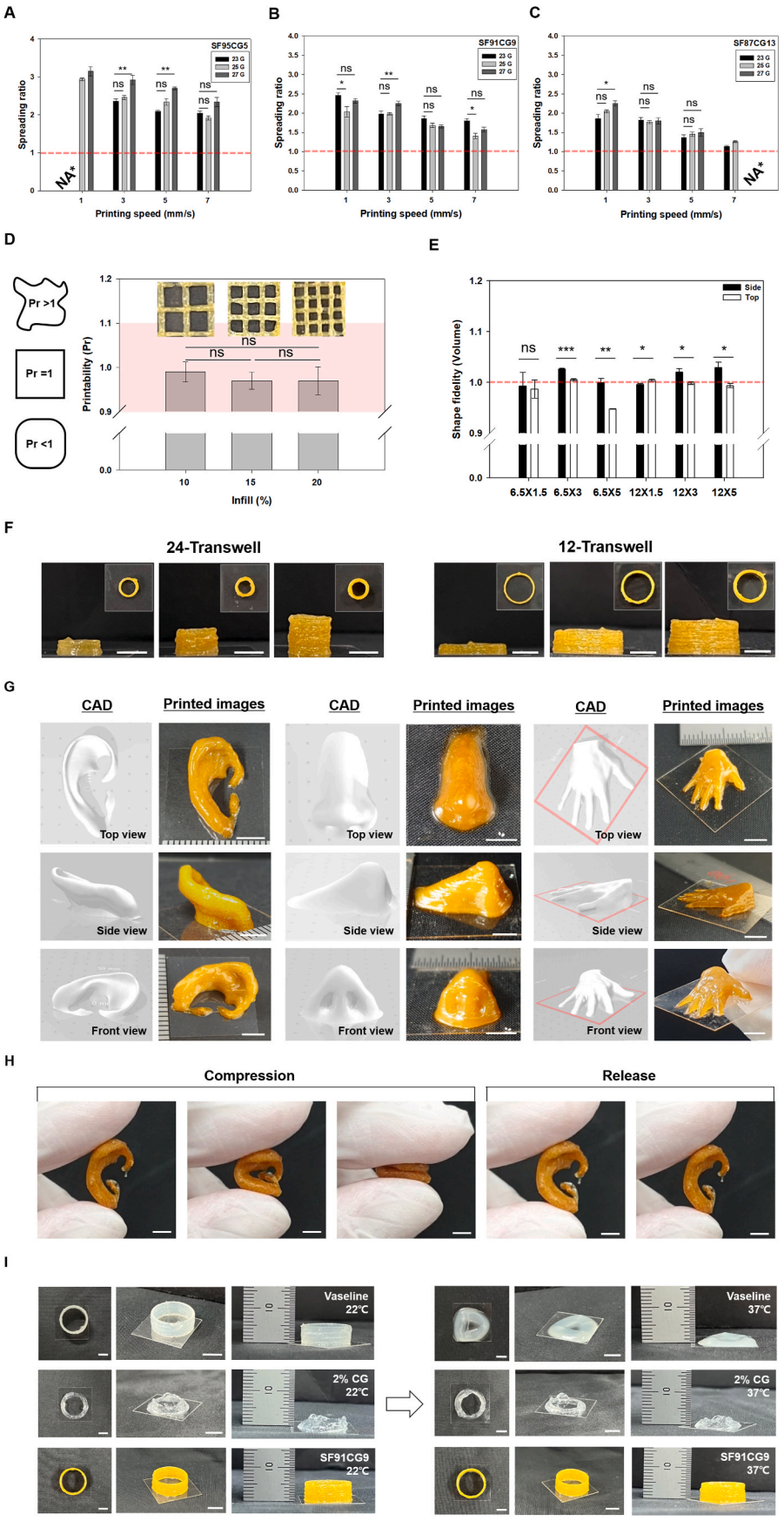

(caption on next page)

Fig. 4. Printability of SF91CG9 using an extrusion-based 3D printer. (A) The spreading ratio varied by nozzle size (0.2 mm, 0.25 mm and 0.33 mm) and printing speeds (1 mm/s, 3 mm/s, 5 mm/s and 7 mm/s) in SF95CG5, (B) SF91CG9, and (C) SF87CG13. (Red dashed line: an ideal spreading ratio, *NA denotes configurations that could not create adequate prints). (D) Quantified Pr value of printed constructs for SF91CG9 with different infill percentages (Red box represented acceptable printability region [116]). (E) Semi-quantified shape fidelity value with printed cylinder structures. (F) 3D Printed constructs based on commercial 12-transwell and 24-transwell diameters with variable heights. (G) CAD images depicting the ear, nose, and hand and printed images at various angles. (H) Compression-release test by hand with 3D ear construct. (I) Comparison of structural stability of printed constructs for Vaseline, 2% CG, and SF91CG9 under different temperature condition (printing temperature 22°C and 37°C). Scale bars indicate 5 mm. All error bars represent the standard deviations (n =3) with statistical significance (*p <0.05, **p <0.01, ***p <0.005, and ns: not significant). (For interpretation of the references to color in this figure legend, the reader is referred to the Web version of this article.)

from over gelation (Fig. S5B). Lower spreading ratio value close to 1 allow fabricate cell-laden scaffolds with higher precision [27]. According to previous studies, mostly natural polymer-based bioinks with using extrusion-based printer presented spreading ratio over 5 or 10, and few of them had range from 2 to 3 [27,114,115]. Overall, the spreading ratio from all of SF/CG bioinks with optimal conditions was around 1 (from 1.9 ± 0.1 to 1.1) due to the irradiation of light to induce rapid dityrosine photo-crosslinking during printing. SF95CG5 showed higher spreading ratio than SF91CG9 and SF87CG13 in all various parameters of printing speed and nozzle size, regarded as relatively low printing resolution. SF87CG13 needed excessive shear forces to be extruded when using lower size of nozzle owing to its high viscosity, leading to nozzle clogging during printing. In this study, SF91CG9 was selected for further printing equipped with 25 G nozzle and printing speed of 5 mm/s.

The fusion of bioink at the cross sites within the lattice structure leads to its collapse, preventing the fabrication of mechanically strong 3D constructs. However, when two subsequent layers are printed using properly gelled bioink, interconnected channels are formed, resulting in a distinct layer with a close-to-square pore shape featuring angular edges instead of chamfers [116]. The squareness of the pores within the grid structures determines the printability value (Pr) [117]. A Pr value of 1 indicates a perfect square shape achieved by appropriately gelled inks that are stacked to form 3D structures with smooth filaments [118]. Conversely, poorly conditioned inks, characterized by irregularly shaped filaments (over-gelation) or a liquid-like consistency (under--gelation), yield Pr values greater than 1 or less than 1, respectively [118,119]. Consequently, 3D printed grid structures exhibiting Pr values ranging from 0.9 to 1.1 demonstrate durable filament morphology and structural stability [116,119]. Fig. 4D illustrates the Pr values of SF91CG9 bioink with varying infill percentages, showing that SF91CG9 can successfully print interconnected channels up to 20% infill without fiber coalescence [91].

To achieve the fabrication of geometrically complex organs, patient-specific constructs, or implants, it is crucial for 3D printed objects to closely resemble the original medical images or computer-designed models [117]. The evaluation of post-fabrication shape fidelity can be partially quantified by comparing the volume of the original objects with that of the printed objects (Fig. 4E). In this study, three variable cylinder structures representing different thicknesses of skin tissue matrices (1.5 mm, 3 mm, and 5 mm, corresponding to epidermal matrix, epidermal-dermal matrix, and the entire thickness of the skin model matrix, respectively [120]) were used to assess the geometrical features (Fig. 4F). The cross-sectional areas of the printed objects were measured from top and side views at various angles and converted into volumetric dimensions [29]. When the printed structures closely matched the ideal objects, the shape fidelity index approached 1. As depicted in Fig. 4E, the shape fidelity values for the variable constructs were all close to 1, indicating high geometric accuracy compared to the original design images.

Printing human organ constructs poses challenges due to their complex and irregular geometries [121]. In this study, replicating the intricate geometries of organs by creating miniature versions of an ear auricle with a curved surface, a nose with nostrils, and an open hand with five fingers, which are typically difficult to print using extrusion-based printing techniques, were conducted. Fig. 4G demonstrates the successful construction of these structures through a layer-by-layer extrusion process, closely resembling the CAD images. Notably, the miniature replica of the ear displayed remarkable resilience and elasticity, enduring pressure from fingers and returning to its original shape without any deformations (Fig. 4H). After the printing process, the printed structures were incubated at 37°C, showcasing their structural stability by maintaining their pre-incubation dimensions. In contrast, constructs printed using Vaseline and sole CG ink collapsed under the same conditions (Fig. 4I). The excellent reproducibility of SF/CG bioink was evident from the deviations, which did not exceed 0.02 across all tested samples, as indicated in Table 2. The 3D printing system achieved significant advancements, enabling the printing of stable and layered structures with heights ranging from 12 to 15 mm (equivalent to 40–50 layers), exemplified by the successful printing of the ear and nose. These achievements demonstrate the challenges overcome by our extrusion-based printing technology using natural polymer-based inks [13,34,122].

3.5. Biocompatibility of the SF/CG scaffolds

The ideal scaffolds used in tissue engineering should facilitate cell adhesion and proliferation, which are critical for regulating the functionality of implanted cells [123]. As shown in Fig. 2, pore sizes and stiffness modulus have an impact on cell-cell interaction and the migration of cells across scaffolds [124]. Here, human keratinocyte HaCaT and myoblast C2C12 cells were selected as suitable cell lines for cultivation on SF/CG scaffolds, aiming to promote skin and muscle tissue regeneration [66]. To assess the cytocompatibility of SF/CG scaffolds with varying CG ratios, a CCK-8 assay was conducted over a span of 3 days, measuring the mean OD 450 value as an indicator of initial cell attachment and growth on the scaffolds. Cell numbers increased in all groups, suggesting that both the SF/CG scaffolds and the native SF provided a favorable microenvironment for cell growth [125]. SF has

Table 2
Parameters of optimization for 3D printing as bioink (SF95CG5, SF91CG9 and SF87CG13). (*NA denotes configurations that could not create adequate prints).

SF/CG ink	Nozzle size (mm)	Printed strand width (mm)			
		Printing speed (mm/s)			
		1 mm/s	3 mm/s	5 mm/s	7 mm/s
SF95CG5	**0.33**	NA*	0.78 (±0.01)	0.69 (±0.01)	0.68 (±0.01)
	0.25	0.74 (±0.01)	0.62 (±0.01)	0.59 (±0.02)	0.48 (±0.01)
	0.2	0.63 (±0.02)	0.59 (±0.02)	0.54 (±0.01)	0.47 (±0.02)
SF91CG9	**0.33**	0.81 (±0.01)	0.65 (±0.02)	0.61 (±0.01)	0.59 (±0.01)
	0.25	0.51 (±0.02)	0.50 (±0.01)	0.42 (±0.01)	0.35 (±0.01)
	0.2	0.46 (±0.01)	0.45 (±0.01)	0.33 (±0.01)	0.32 (±0.01)
SF87CG13	**0.33**	0.61 (±0.02)	0.60 (±0.02)	0.45 (±0.02)	0.38 (±0.01)
	0.25	0.51 (±0.01)	0.44 (±0.01)	0.36 (±0.01)	0.32
	0.2	0.45 (±0.01)	0.36 (±0.01)	0.3 (±0.01)	NA*

been widely recognized as an excellent biocompatible material and extensively studied for various biomedical applications over the years [126,127].

Fig. 5A showed addition of CG enhanced the initial attachment of C2C12 cells compared to sole SF. After two days of incubation, the proliferative rate of HaCaT cells in the SF/CG experimental groups (SF95CG5, SF91CG9, and SF87CG13) began to surpass that of the SF alone. By day 3, the proliferation in SF91CG9 and SF95CG5 was significantly higher than the other groups. Regarding HaCaT cells, there were no significant differences in adhesion among all the groups on the first day (Fig. 5B). However, SF95CG5 exhibited remarkable performance, with adhesion levels 2.3-times higher than the other groups by day 3, followed by SF91CG9 with a 1.3-fold increase. These results indicate that dual-crosslinked SF/CG scaffolds with an optimal CG ratio have the advantage of enhancing cell adhesion and proliferation of myoblasts and keratinocytes, attributable to the micro-porosity, hydrophilicity, and stiffness modulus of the scaffolds [128].

To ensure the homogeneous printing of encapsulated cells and ink

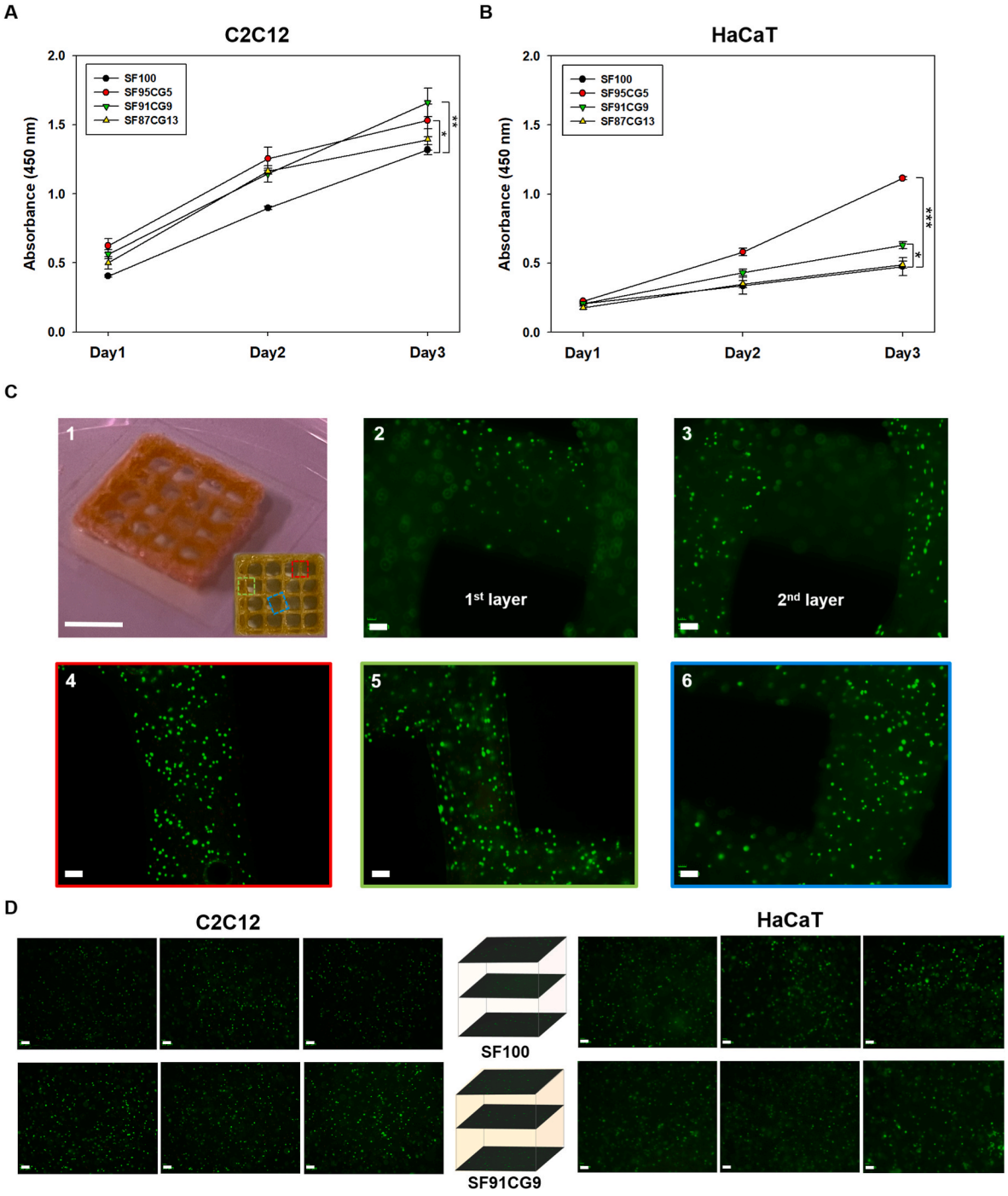

Fig. 5. Cytocompatibility of SG/CG. CCK-8 results of (A) C2C12 cells and (B) HaCaT. (C) Live/dead staining of myoblast-laden SF91CG9 lattice constructs cultured for three days after printing (Locations of Fig. 5C4-6 are marked with red, green, and blue dashed boxes, respectively in Fig. 5C1) (D) Live/dead staining of the 3D bioprinted C2C12 and HaCaT cell-laden scaffolds on day 3 (SF100 and SF91CG9). Scale bars indicate 5 mm in (C.1) and 100 μm in (C.2-6) and (D). All error bars represent the standard deviations (n =3) with statistical significance (*p <0.05, **p <0.01, and ***p <0.005). (For interpretation of the references to color in this figure legend, the reader is referred to the Web version of this article.)

materials, it is crucial to extrude the ink from the nozzles with minimal applied shear force [129]. During the printing process, the dispensing pressure from the piston can potentially harm the loaded cells, compromising their viability in the printed products [130,131]. To evaluate the impact of the bioprinting process on the cell viability of cell-laden structures, viability was assessed using representative merged fluorescent images of live/dead staining to visualize the spatial gradient of the printed structures. Live cells were stained in green, while dead cells were stained in red. Considering both printability and biocompatibility, SF91CG9 was selected as the optimal bioink among the SF/CG formulations and was used for the experimental group.

As shown in Fig. 5C, the printing process resulted in minimal cell death, and cells were uniformly distributed along the streak line of the ink matrix without any clumping. Furthermore, the appearance of cells was distinguishable in each layer, as evidenced by the z-axis stack of images in bilayer structures, indicating the ability to deliver cells to the intended positions. Three days after printing and incubation under normal culture conditions, cell viability within the printed structures (SF100 and SF91CG9) was analyzed to assess whether the presence of CG in the scaffolds affected cell-ink material interactions (Fig. S6) [132]. As depicted in Fig. 5D, the predominant green fluorescence, representing a high population of live C2C12 and HaCaT cells, indicated that there were minimal dead cells in both SF100 and SF91CG9. The cell viability within the printed structures of SF91CG9 on day 3 was calculated and showed the enhancement in both C2C12 and HaCaT with 97.8 $\pm$ 0.5% and 95.6 $\pm$ 1.4% respectively, compared to that of SF100, 91.5 $\pm$ 1.7 % and 88.5 $\pm$ 1.1 % (Fig. S7). Especially, the maximum cell viability of SF91CG9 loaded with C2C12 were 98.3%, which was higher than that of conventional bioinks using extrusion-based bioprinting [133,134]. From these results, the addition of CG to bioinks do not any harmful effect on the encapsulated cells, but rather ensure favorable cell viability and minimal cytotoxicity [78,135,136]. Therefore, SF91CG9 is a desirable candidate for extrusion-based printing, as it exhibits superior printability [115]. Moreover, scaffolds incorporating CG are expected to positively influence specific cell attachment and provide an appropriate growth environment for keratinocytes and myoblasts, making them suitable for applications in corneal, skin, and muscle tissue engineering [137–139].

Aging and disease can alter tissue stiffness, which in turn affects cellular function and phenotypic variation [67,140,141]. In order to develop personalized medicine without limitations imposed by aging and disease, it is essential to have the ability to adjust the mechanical and physical properties of 3D constructs. Moreover, the incorporation of scaffolds with varying stiffness levels enables the simultaneous containment of multiple cells, facilitating aggregate formation and differentiation in specific directions. This feature can be applied in 3D cell culture technologies for high-throughput drug discovery and disease modeling [142,143].

3.6. Biodegradability of the SF/CG scaffolds

Degradability of the printed constructs are essential requirement for the success of scaffold in tissue engineering [27]. It is important for the constructs to degrade within the implanted site at a rate equivalent to cell growth, allowing for tissue formation and avoiding the need for a second surgical intervention for removal. The constructs should also provide continuous support during the gradual regeneration process [122,144]. If natural materials degrade rapidly in the physiological environment, they may lose mechanical strength, leading to collapse and failure to serve their intended purpose [145]. In the case of skin and skeletal muscle tissue regeneration, slowly degrading scaffolds that maintain their integrity for 4–8 weeks are required to allow sufficient time for the repair process of the implanted construct [144–146].

Cells encapsulated within scaffolds produce and secrete various proteolytic enzymes, which can contribute to scaffold degradation [147]. Therefore, degradation tests should be conducted by monitoring the weight loss of the constructs during 28 days of incubation at 37°C under two parallel conditions: hydrolytic and enzymatic [148]. Protease XIV was chosen for the enzymatic treatment, as it has the ability to randomly cleave silk fibroin at multiple locations, supported by previous evidence [149,150]. From Fig. 6A, the SF/CG constructs exhibited minimal degradation (7–8% weight loss) over 28 days in the hydrolytic condition, while SF100 experienced a reduction in mass of approximately 20%. During degradation by the protease, SF100 showed the highest reduction in mass, reaching a maximum of 37%, while SF95CG5 and SF91CG9 exhibited reductions of approximately 28% and 17% in mass, respectively (Fig. 6B). However, SF87CG13 displayed no significant difference in degradation rate between the hydrolytic and enzymatic conditions, as it lacked effective sites for protease cleavage [145]. In addition, the weight increment of SF87CG13 was observed on day 3 in presence of protease XIV. This phenomenon might have been due to the formation of pores and changes in crosslinked structure, originated from the part of the degraded SF, followed by the formed pores inside the network were filled with the water-molecule [151].

Surface contraction modifies seeded cell behavior [152]. To evaluate the surface area contraction of SF/CG scaffolds during the culture period, the constructs were incubated under enzymatic conditions for 28 days. As shown in Fig. 6C and D, the incorporation of CG in the scaffolds prevented surface area contraction compared to SF100, which experienced a contraction of 77 $\pm$ 3% of the initial surface area. Previous studies have demonstrated that the epidermal portion of common skin models is susceptible to contraction caused by fibroblasts, resulting in 80% contraction within 15 days, which poses a challenge in terms of reproducibility [152,153]. However, SF91CG9 and SF87CG13 exhibited no contraction over 15 days, maintaining their surface areas at 100%. Based on these results, along with the capability to print within transwell diameters (as shown in Fig. 4F), SF/CG blended bioink could be expoloited for the fabrication of a non-shrinkable scaffold.

Thus, incorporation of CG in scaffolds not only supports cell viability without disrupting the constructs but also prevents surface contraction during the culture period. To exert its advantage, CG should remain in the SF/CG blended scaffolds for the intended duration and conditions. To assess the release of CG, the incubated eluates from two parallel groups (37°C, normal *in vitro* temperature, and 60°C, the melting temperature of iota CG) were collected to determine the total CG content using the phenol-sulfuric acid method [154,155]. The released CG from each sample was quantitatively measured using a standard curve with glucose as a reference [156]. No carbohydrates were detected in the SF100 sample, confirming that this method is suitable for the quantitative analysis of CG only (data not shown). From the constructs with a higher CG ratio, a greater amount of carrageenan was released at 60°C, approximately 40% of the initial amounts in SF87CG13 (Fig. 6E). However, no CG release was observed when the samples were incubated at 37°C for all SF/CG blended groups over the 4-week duration (Fig. 6F). Overall, the long-term retention of CG in complementary network SF/CG scaffolds facilitates the modulation of bioprinted cell behavior and tissue formation, providing the desired period of use for potential applications in 3D tissue regeneration of skin and muscle (4–8 weeks) [144,146].

4. Conclusion

In this study, temperature and light-induced printable blends of SF and CG were developed for desirable bioink for extrusion-based printing. The inclusion of CG enhanced the thermo-responsive gelling ability, resulting in improved viscoelastic properties. Additionally, the visible light-activated dityrosine crosslinking of SF enabled immediate curing of the matrix layer when the ink was extruded from the nozzle orifice. This novel combination of SF and CG provided high printability with excellent shape fidelity and structural stability under physiological conditions, surpassing the capabilities of sole SF or CG bioinks. Self-standing 3D constructs with various scale, including ear auricle, nose

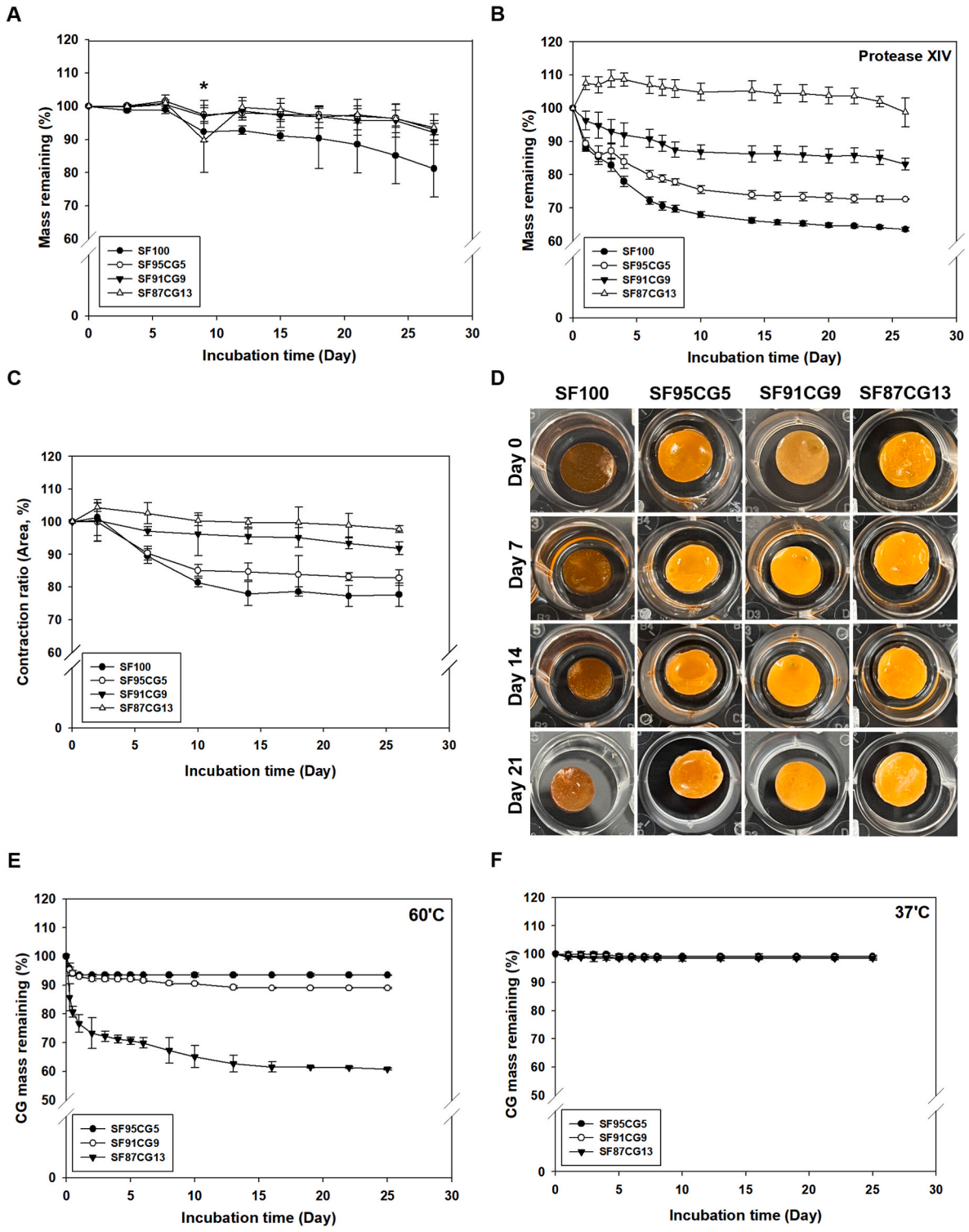

Fig. 6. Biodegradability of SF/CG scaffolds. *In vitro* degradation rate of SF/CG scaffolds in (A) PBS and (B) protease XIV. (* Weight of samples were recorded lower than expected owing to dry issues of immersing solution, leading to dehydration of gel.) (C) Surface area contraction ratio of SF/CG scaffolds incubated in protease XIV and (D) their representative pictures of SF/CG scaffolds obtained by every week. Quantitative analysis of CG from eluate incubated in (E) 60°C and (F) 37°C.

with nostril, hand with five fingers open and cylinder applied in transwell, could be successfully manufactured without the assist of sacrificial bath.

The SF/CG bioink allowed for homogeneous distribution of live cells during extrusion, without compromising cell viability. Furthermore, the 3D bioprinted constructs facilitated cellular adhesion and proliferation of HaCaT and C2C12 cells. This effect can be attributed to the adjustable micropore sizes, favorable surface wettability, hydrated microenvironments, and structural integrity of the SF/CG scaffolds, which prevented excessive contraction during 21 days of culture.

In summary, the dual-crosslinking strategy employed in SF/CG bioink successfully reconciles the conflicting requirements of superior printability with appropriate rheological properties and functional performance with a desirable microenvironment. Moreover, this

approach overcomes the limited mechanical durability of existing ink materials composed solely of naturally derived biomaterials. The superior shape fidelity and reproducibility, along with minimal volumetric shrinkage observed in SF/CG bioink, open up possibilities for CAD-assisted patient-specific therapeutic alternatives and the development of *in vitro* models for skin, cornea, bladder, and skeletal substitutes. Collectively, the proposed SF/CG bioink demonstrates enormous potential for manufacturing complex bioprinted 3D constructs in a wide range of tissue engineering applications, including personalized therapy, regenerative medicine, preclinical trials for specific tissues, and soft robotics.

CRediT authorship contribution statement

Seo Hyung Moon: Writing – review & editing, Writing – original draft, Visualization, Validation, Investigation. **Tae Yoon Park:** Visualization, Investigation. **Hyung Joon Cha:** Writing – review & editing, Supervision, Funding acquisition, Conceptualization. **Yun Jung Yang:** Writing – review & editing, Writing – original draft, Visualization, Supervision, Funding acquisition, Conceptualization.

Declaration of competing interest

The authors declare the following financial interests/personal relationships which may be considered as potential competing interests: Yun Jung Yang reports financial support was provided by Ministry of Science and ICT, Korea. Yun Jung Yang reports financial support was provided by Korea Institute of Marine Science & Technology Promotion (KIMST) funded by the Ministry of Oceans and Fisheries, Korea.

Data availability

No data was used for the research described in the article.

Acknowledgements

The authors acknowledge the financial support from the basic science research program (NRF-2020R1C1C1006737) funded by the Ministry of Science and ICT, Korea; Development of marine de-rived polymer for 3D bioink' (KIMST-20200354) of Korea Institute of Marine Science & Technology Promotion (KIMST) funded by the Ministry of Oceans and Fisheries, Korea.

Appendix A. Supplementary data

Supplementary data to this article can be found online at https://doi.org/10.1016/j.mtbio.2024.100973.

References

[1] N. Shahrubudin, T.C. Lee, R. Ramlan, An overview on 3D printing technology: technological, materials, and applications, Procedia Manuf. 35 (2019) 1286–1296, https://doi.org/10.1016/j.promfg.2019.06.089.
[2] N. Nachal, J.A. Moses, P. Karthik, C. Anandharamakrishnan, Applications of 3D printing in food processing, Food Eng. Rev. 11 (2019) 123–141, https://doi.org/10.1007/s12393-019-09199-8.
[3] Z. Chen, Z. Li, J. Li, C. Liu, C. Lao, Y. Fu, C. Liu, Y. Li, P. Wang, Y. He, 3D printing of ceramics: a review, J. Eur. Ceram. Soc. 39 (2019) 661–687, https://doi.org/10.1016/j.jeurceramsoc.2018.11.013.
[4] H. Wang, J.Y. Lim, Metal-ceramic bond strength of a cobalt chromium alloy for dental prosthetic restorations with a porous structure using metal 3D printing, Comput. Biol. Med. 112 (2019) 103364, https://doi.org/10.1016/j.compbiomed.2019.103364.
[5] S.H. Moon, H.N. Choi, Y.J. Yang, Natural/synthetic polymer materials for bioink development, Biotechnol. Bioproc. Eng. 27 (2022) 482–493, https://doi.org/10.1007/s12257-021-0418-1.
[6] H. Tetsuka, S. Ryon Shin, Materials and technical innovations in 3D printing in biomedical applications, J. Mater. Chem. B 8 (2020) 2930–2950, https://doi.org/10.1039/d0tb00034e.
[7] S. You, Y. Xiang, H.H. Hwang, D.B. Berry, W. Kiratitanaporn, J. Guan, E. Yao, M. Tang, Z. Zhong, X. Ma, D. Wangpraseurt, Y. Sun, T.Y. Lu, S. Chen, High cell density and high-resolution 3D bioprinting for fabricating vascularized tissues, Sci. Adv. 9 (2023) eade7923, https://doi.org/10.1126/sciadv.ade7923.
[8] Y. Fang, Y. Guo, M. Ji, B. Li, Y. Guo, J. Zhu, T. Zhang, Z. Xiong, 3D Printing of cell-laden microgel-based biphasic bioink with heterogeneous microenvironment for biomedical applications, Adv. Funct. Mater. 32 (2022) 2109810, https://doi.org/10.1002/adfm.202109810.
[9] P.S. Gungor-Ozkerim, I. Inci, Y.S. Zhang, A. Khademhosseini, M.R. Dokmeci, Bioinks for 3D bioprinting: an overview, Biomater. Sci. 6 (2018) 915–946, https://doi.org/10.1039/c7bm00765e.
[10] R. Pugliese, B. Beltrami, S. Regondi, C. Lunetta, Polymeric biomaterials for 3D printing in medicine: an overview, Ann. 3D Print. Med. 2 (2021) 100011, https://doi.org/10.1016/j.stlm.2021.100011.
[11] G. Choi, H.J. Cha, Recent advances in the development of nature-derived photocrosslinkable biomaterials for 3D printing in tissue engineering, Biomater. Res. 23 (2019), https://doi.org/10.1186/S40824-019-0168-8.
[12] R. Khoeini, H. Nosrati, A. Akbarzadeh, A. Eftekhari, T. Kavetskyy, R. Khalilov, E. Ahmadian, A. Nasibova, P. Datta, L. Roshangar, D.C. Deluca, S. Davaran, M. Cucchiarini, I.T. Ozbolat, Natural and synthetic bioinks for 3D bioprinting, Adv. NanoBiomed Res. 1 (2021) 2000097, https://doi.org/10.1002/anbr.202000097.
[13] H. Kim, B. Kang, X. Cui, S.H. Lee, K. Lee, D.W. Cho, W. Hwang, T.B.F. Woodfield, K.S. Lim, J. Jang, Light-activated decellularized extracellular matrix-based bioinks for volumetric tissue analogs at the centimeter scale, Adv. Funct. Mater. 31 (2021) 2011252, https://doi.org/10.1002/adfm.202011252.
[14] R. Levato, T. Jungst, R.G. Scheuring, T. Blunk, J. Groll, J. Malda, From shape to function: the next step in bioprinting, Adv. Mater. 32 (2020) 1906423, https://doi.org/10.1002/adma.201906423.
[15] J.K. Placone, A.J. Engler, Recent advances in extrusion-based 3D printing for biomedical applications, Adv. Healthcare Mater. 7 (2018) e1701161, https://doi.org/10.1002/adhm.201701161.
[16] R.F. Pereira, A. Sousa, C.C. Barrias, P.J. Bártolo, P.L. Granja, A single-component hydrogel bioink for bioprinting of bioengineered 3D constructs for dermal tissue engineering, Mater. Horiz. 5 (2018) 1100–1111, https://doi.org/10.1039/c8mh00525g.
[17] H.J. Jeong, H. Nam, J. Jang, S.J. Lee, 3D bioprinting strategies for the regeneration of functional tubular tissues and organs, Bioengineering 7 (2020) 32, https://doi.org/10.3390/bioengineering7020032.
[18] T. Zhang, W. Zhao, Z. Xiahou, X. Wang, K. Zhang, J. Yin, Bioink design for extrusion-based bioprinting, Appl. Mater. Today 25 (2021) 101227, https://doi.org/10.1016/j.apmt.2021.101227.
[19] I.M. Lei, Y. Sheng, C.L. Lei, C. Leow, Y.Y.S. Huang, A hackable, multi-functional, and modular extrusion 3D printer for soft materials, Sci. Rep. 12 (2022) 12294, https://doi.org/10.1038/s41598-022-16008-6.
[20] M. Pitton, A. Fiorati, S. Buscemi, L. Melone, S. Farè, N. Contessi Negrini, 3D Bioprinting of pectin-cellulose nanofibers multicomponent bioinks, Front. Bioeng. Biotechnol. 9 (2021) 732689, https://doi.org/10.3389/fbioe.2021.732689/bibtex.
[21] S.H. Moon, H.J. Hwang, H.R. Jeon, S.J. Park, I.S. Bae, Y.J. Yang, Photocrosslinkable natural polymers in tissue engineering, Front. Bioeng. Biotechnol. 11 (2023) 1127757, https://doi.org/10.3389/fbioe.2023.1127757.
[22] A.M. Compaan, K. Christensen, Y. Huang, Inkjet bioprinting of 3D silk fibroin cellular constructs using sacrificial alginate, ACS Biomater. Sci. Eng. 3 (2017) 1519–1526, https://doi.org/10.1021/acsbiomaterials.6b00432.
[23] H. Rastin, B. Zhang, J. Bi, K. Hassan, T.T. Tung, D. Losic, 3D printing of cell-laden electroconductive bioink for tissue engineering Application, J. Mater. Chem. B 8 (2020) 5862–5876, https://doi.org/10.1039/d0Tb00627k.
[24] J.I. González Ocampo, M.M. Machado de Paula, N.J. Bassous, A.O. Lobo, C. P. Ossa Orozco, T.J. Webster, Osteoblast responses to injectable bone substitutes of kappa-carrageenan and nano hydroxyapatite, Acta Biomater. 83 (2019) 425–434, https://doi.org/10.1016/j.actbio.2018.10.023.
[25] H. Zhang, L. ling Li, F. yin Dai, H. hao Zhang, B. Ni, W. Zhou, X. Yang, Y. zhang Wu, Preparation and characterization of silk fibroin as a biomaterial with potential for drug delivery, J. Transl. Med. 10 (2012) 117, https://doi.org/10.1186/1479-5876-10-117.
[26] H. Dou, B. Zuo, Effect of sodium carbonate concentrations on the degumming and regeneration process of silk fibroin, J. Text. Inst. 106 (2015) 311–319, https://doi.org/10.1080/00405000.2014.919065.
[27] F.E. Freeman, D.J. Kelly, Tuning alginate bioink stiffness and composition for controlled growth factor delivery and to spatially direct MSC fate within bioprinted Tissues, Sci. Rep. 7 (2017) 17042, https://doi.org/10.1038/S41598-017-17286-1.
[28] M. Machour, N. Hen, I. Goldfracht, D. Safina, M. Davidovich-Pinhas, H. Bianco-Peled, S. Levenberg, Print-and-grow within a novel support material for 3D bioprinting and post-printing tissue Growth, Adv. Sci. 9 (2022) 2200882, https://doi.org/10.1002/advs.202200882.
[29] M. Hua, D. Wu, S. Wu, Y. Ma, Y. Alsaid, X. He, 4D printable tough and thermoresponsive hydrogels, ACS Appl. Mater. Interfaces 13 (2021) 12689–12697, https://doi.org/10.1021/acsami.0c17532.
[30] X. Cui, B.G. Soliman, C.R. Alcala-Orozco, J. Li, M.A.M. Vis, M. Santos, S.G. Wise, R. Levato, J. Malda, T.B.F. Woodfield, J. Rnjak-Kovacina, K.S. Lim, Rapid photocrosslinking of silk hydrogels with high cell density and enhanced shape fidelity, Adv. Healthcare Mater. 9 (2020) 1901667, https://doi.org/10.1002/adhm.201901667.
[31] K.M. Zadeh, A.S. Luyt, L. Zarif, R. Augustine, A. Hasan, M. Messori, M.K. Hassan, H.C. Yalcin, Electrospun polylactic acid/date palm polyphenol extract nanofibres

for tissue engineering applications, Emergent Mater 2 (2019) 141–151, https://doi.org/10.1007/s42247-019-00042-8.
[32] H.J. Jang, M.S. Kang, W.H. Kim, H.J. Jo, S.H. Lee, E.J. Hahm, J.H. Oh, S.W. Hong, B. Kim, D.W. Han, 3D printed membranes of polylactic acid and graphene oxide for guided bone regeneration, Nanoscale Adv. 5 (2023) 3619–3628, https://doi.org/10.1039/d3na00112a.
[33] O. Hasturk, K.E. Jordan, J. Choi, D.L. Kaplan, Enzymatically crosslinked silk and silk-gelatin hydrogels with tunable gelation kinetics, mechanical properties and bioactivity for cell culture and encapsulation, Biomaterials 232 (2020) 119720, https://doi.org/10.1016/j.biomaterials.2019.119720.
[34] S.H. Kim, Y.K. Yeon, J.M. Lee, J.R. Chao, Y.J. Lee, Y.B. Seo, M.T. Sultan, O.J. Lee, J.S. Lee, S. Yoon, I.S. Hong, G. Khang, S.J. Lee, J.J. Yoo, C.H. Park, Precisely printable and biocompatible silk fibroin bioink for digital light processing 3D printing, Nat. Commun. 9 (2018) 1620, https://doi.org/10.1038/s41467-018-03759-y.
[35] I.C. Um, H.Y. Kweon, Y.H. Park, S. Hudson, Structural characteristics and properties of the regenerated silk fibroin prepared from formic acid, Int. J. Biol. Macromol. 29 (2001) 91–97, https://doi.org/10.1016/a0141-8130(01)00159-3.
[36] D. Gong, Q. Lin, Z. Shao, X. Chen, Y. Yang, Preparing 3D-printable silk fibroin hydrogels with robustness by a two-step crosslinking method, RSC Adv. 10 (2020) 27225–27234, https://doi.org/10.1039/d0ra04789a.
[37] X. Du, D. Wei, L. Huang, M. Zhu, Y. Zhang, Y. Zhu, 3D printing of mesoporous bioactive glass/silk fibroin composite scaffolds for bone tissue engineering, Mater. Sci. Eng. C 103 (2019) 109731, https://doi.org/10.1016/j.msec.2019.05.016.
[38] J. Liu, M. Shahriar, H. Xu, C. Xu, Cell-laden bioink circulation-assisted inkjet-based bioprinting to mitigate cell sedimentation and aggregation, Biofabrication 14 (2022) 045020, https://doi.org/10.1088/1758-5090/ac8fb7.
[39] B.P. Partlow, M.B. Applegate, F.G. Omenetto, D.L. Kaplan, Dityrosine cross-linking in designing biomaterials, ACS Biomater. Sci. Eng. 2 (2016) 2108–2121, https://doi.org/10.1021/acsbiomaterials.6b00454.
[40] C. Liu, J. Hua, P.F. Ng, B. Fei, Photochemistry of bioinspired dityrosine crosslinking, J. Mater. Sci. Technol. 63 (2021) 182–191, https://doi.org/10.1016/j.jmst.2020.02.086.
[41] J.L. Whittaker, N.R. Choudhury, N.K. Dutta, A. Zannettino, Facile and rapid ruthenium mediated photo-crosslinking of Bombyx mori silk fibroin, J. Mater. Chem. B 2 (2014) 6259–6270, https://doi.org/10.1039/c4tb00698d.
[42] E. Ruggiero, S.A. Castro, A. Habtemariam, L. Salassa, Upconverting nanoparticles for the near infrared photoactivation of transition metal complexes: new opportunities and challenges in medicinal inorganic photochemistry, Dalton Trans. 45 (2016) 13012–13020, https://doi.org/10.1039/c6dt01428c.
[43] B.P. Partlow, C.W. Hanna, J. Rnjak-Kovacina, J.E. Moreau, M.B. Applegate, K. A. Burke, B. Marelli, A.N. Mitropoulos, F.G. Omenetto, D.L. Kaplan, Highly tunable elastomeric silk biomaterials, Adv. Funct. Mater. 24 (2014) 4615–4624, https://doi.org/10.1002/adfm.201400526.
[44] S. Sakai, H. Kamei, T. Mori, T. Hotta, H. Ohi, M. Nakahata, M. Taya, Visible light-induced hydrogelation of an alginate derivative and application to stereolithographic bioprinting using a visible light projector and acid red, Biomacromolecules 19 (2018) 672–679, https://doi.org/10.1021/acs.biomac.7b01827.
[45] K.S. Lim, B.S. Schon, N.V. Mekhileri, G.C.J. Brown, C.M. Chia, S. Prabakar, G. J. Hooper, T.B.F. Woodfield, New visible-light photoinitiating system for improved print fidelity in gelatin-based bioinks, ACS Biomater. Sci. Eng. 2 (2016) 1752–1762, https://doi.org/10.1021/acsbiomaterials.6b00149.
[46] P. Atienza-Roca, D.C. Kieser, X. Cui, B. Bathish, Y. Ramaswamy, G.J. Hooper, A. N. Clarkson, J. Rnjak-Kovacina, P.J. Martens, L.M. Wise, T.B.F. Woodfield, K. S. Lim, Visible light mediated PVA-tyramine hydrogels for covalent incorporation and tailorable release of functional growth factors, Biomater. Sci. 8 (2020) 5005–5019, https://doi.org/10.1039/d0bm00603c.
[47] X. Mu, J.K. Sahoo, P. Cebe, D.L. Kaplan, Photo-crosslinked silk fibroin for 3D printing, Polymers 12 (2020) 2936, https://doi.org/10.3390/polym12122936.
[48] K.A. Deo, K.A. Singh, C.W. Peak, D.L. Alge, A.K. Gaharwar, Bioprinting 101: design, fabrication, and evaluation of cell-laden 3D bioprinted scaffolds, Tissue Eng. 26 (2020) 318–338, https://doi.org/10.1089/ten.tea.2019.0298.
[49] L. Schefer, I. Usov, R. Mezzenga, Anomalous stiffening and ion-induced coil-helix transition of carrageenans under monovalent salt conditions, Biomacromolecules 16 (2015) 985–991, https://doi.org/10.1021/bm501874k.
[50] S.A. Wilson, L.M. Cross, C.W. Peak, A.K. Gaharwar, Shear-thinning and thermo-reversible nanoengineered inks for 3D bioprinting, ACS Appl. Mater. Interfaces 9 (2017) 43449–43458, https://doi.org/10.1021/acsami.7b13602.
[51] P. Zhuang, W.L. Ng, J. An, C.K. Chua, L.P. Tan, Layer-by-layer ultraviolet assisted extrusion-based (UAE) bioprinting of hydrogel constructs with high aspect ratio for soft tissue engineering applications, PLoS One 14 (2019) e0216776, https://doi.org/10.1371/journal.pone.0216776.
[52] Q.L. Loh, C. Choong, Three-dimensional scaffolds for tissue engineering applications: role of porosity and pore size, Tissue Eng., Part B 19 (2013) 485–502, https://doi.org/10.1089/ten.teb.2012.0437.
[53] M. Ferrari, F. Cirisano, M. Carmen Morán, Mammalian cell behavior on hydrophobic substrates: influence of surface properties, Colloids Interfaces 3 (2019) 48, https://doi.org/10.3390/colloids3020048.
[54] S.M. Oliveira, N.M. Alves, J.F. Mano, Cell interactions with superhydrophilic and superhydrophobic surfaces, J. Adhes. Sci. Technol. 28 (2014) 843–863, https://doi.org/10.1080/01694243.2012.697776.
[55] A.S. Hoffman, Hydrogels for biomedical applications, Adv. Drug Deliv. Rev. 64 (2012) 18–23, https://doi.org/10.1016/j.addr.2012.09.010.
[56] M. Ahmed, T.A. da S. Ramos, F. Damanik, B. Quang Le, P. Wieringa, M. Bennink, C. van Blitterswijk, J. de Boer, L. Moroni, A combinatorial approach towards the design of nanofibrous scaffolds for chondrogenesis, Sci. Rep. 5 (2015) 14804, https://doi.org/10.1038/srep14804.
[57] V. Dhyani, N. Singh, Controlling the cell adhesion property of silk films by graft polymerization, ACS Appl. Mater. Interfaces 6 (2014) 5005–5011, https://doi.org/10.1021/am4060595.
[58] S. Cai, C. Wu, W. Yang, W. Liang, H. Yu, L. Liu, Recent advance in surface modification for regulating cell adhesion and behaviors, Nanotechnol. Rev. 9 (2020) 971–989, https://doi.org/10.1515/ntrev-2020-0076.
[59] B. Valamehr, S.J. Jonas, J. Polleux, R. Qiao, S. Guo, E.H. Gschweng, B. Stiles, K. Kam, T.J.M. Luo, O.N. Witte, X. Liu, B. Dunn, H. Wu, Hydrophobic surfaces for enhanced differentiation of embryonic stem cell-derived embryoid bodies, Proc. Natl. Acad. Sci. USA 105 (2008) 14459–14464, https://doi.org/10.1073/pnas.0807235105.
[60] L. Cunha, A. Grenha, Sulfated seaweed polysaccharides as multifunctional materials in drug delivery applications, Mar. Drugs 14 (2016) 42, https://doi.org/10.3390/md14030042.
[61] J.L. Drury, D.J. Mooney, Hydrogels for tissue engineering: scaffold design variables and applications, Biomaterials 24 (2003) 4337–4351, https://doi.org/10.1016/s0142-9612(03)00340-5.
[62] M.S. Nasim Annabi, J.W. Nichol, X. Zhong, C. Ji, S. Koshy, A. Khademhosseini, F. Dehghani, Controlling the porosity and microarchitecture of hydrogels for tissue engineering, Tissue Eng., Part B 16 (2010) 371–383, https://doi.org/10.1089/ten.teb.2009.0639.
[63] N. Abbasi, S. Hamlet, R.M. Love, N.T. Nguyen, Porous scaffolds for bone regeneration, J. Sci. Adv. Mater. Devices. 5 (2020) 1–9, https://doi.org/10.1016/j.jsamd.2020.01.007.
[64] B.B. Mandal, S.C. Kundu, Osteogenic and adipogenic differentiation of rat bone marrow cells on non-mulberry and mulberry silk gland fibroin 3D scaffolds, Biomaterials 30 (2009) 5019–5030, https://doi.org/10.1016/j.biomaterials.2009.05.064.
[65] I.V. Yannas, E. Lee, D.P. Orgill, E.M. Skrabut, G.F. Murphy, Synthesis and characterization of a model extracellular matrix that induces partial regeneration of adult mammalian skin, Proc. Natl. Acad. Sci. USA 86 (1989) 933–937, https://doi.org/10.1073/pnas.86.3.933.
[66] C.F. Guimarães, L. Gasperini, A.P. Marques, R.L. Reis, The stiffness of living tissues and its implications for tissue engineering, Nat. Rev. Mater. 5 (2020) 351–370, https://doi.org/10.1038/s41578-019-0169-1.
[67] Y.D. Nokoorani, A. Shamloo, M. Bahadoran, H. Moravvej, Fabrication and characterization of scaffolds containing different amounts of allantoin for skin tissue engineering, Sci. Rep. 11 (2021) 16164, https://doi.org/10.1038/s41598-021-95763-4.
[68] A.M. Handorf, Y. Zhou, M.A. Halanski, W.-J. Li, Tissue stiffness dictates development, homeostasis, and disease progression, Organogenesis 11 (2015) 1–15, https://doi.org/10.1080/15476278.2015.1019687.
[69] N. Chaicharoenaudomrung, P. Kunhorm, P. Noisa, Three-dimensional cell culture systems as an in vitro platform for cancer and stem cell modeling, World J. Stem Cell. 11 (2019) 1065–1083, https://doi.org/10.4252/wjsc.v11.i12.1065.
[70] M.Y.M. Chiang, Y. Yangben, N.J. Lin, J.L. Zhong, L. Yang, Relationships among cell morphology, intrinsic cell stiffness and cell-substrate interactions, Biomaterials 34 (2013) 9754–9762, https://doi.org/10.1016/j.biomaterials.2013.09.014.
[71] T. Yeung, P.C. Georges, L.A. Flanagan, B. Marg, M. Ortiz, M. Funaki, N. Zahir, W. Ming, V. Weaver, P.A. Janmey, Effects of substrate stiffness on cell morphology, cytoskeletal structure, and adhesion, Cell Motil Cytoskeleton 60 (2005) 24–34, https://doi.org/10.1002/cm.20041.
[72] L. Wang, C. Wang, S. Wu, Y. Fan, X. Li, Influence of the mechanical properties of biomaterials on degradability, cell behaviors and signaling pathways: current progress and challenges, Biomater. Sci. 8 (2020) 2714–2733, https://doi.org/10.1039/d0bm00269k.
[73] M. d'Angelo, E. Benedetti, M.G. Tupone, M. Catanesi, V. Castelli, A. Antonosante, A. Cimini, The role of stiffness in cell reprogramming: a potential role for biomaterials in inducing tissue regeneration, Cell 8 (2019) 1036, https://doi.org/10.3390/cells8091036.
[74] S. Budday, T.C. Ovaert, G.A. Holzapfel, P. Steinmann, E. Kuhl, Fifty shades of brain: a review on the mechanical testing and modeling of brain tissue, Arch. Comput. Methods Eng. 27 (2020) 1187–1230, https://doi.org/10.1007/s11831-019-09352-w.
[75] V. Sabapathy, M. Hurakadli, D. Rana, M. Ramalingam, S. Kumar, Decellularized amniotic membrane scaffold compared to synthetic PLGA and hybrid scaffolds exhibit superlative biomechanical properties for tissue engineering applications, J. Biomater. Tissue Eng. 6 (2016) 549–562, https://doi.org/10.1166/jbt.2016.1480.
[76] O. Janoušková, Synthetic polymer scaffolds for soft tissue engineering, Physiol. Res. 67 (2018) 335–348, https://doi.org/10.33549/physiolres.933983.
[77] V.T.N.T. Bui, B.T. Nguyen, T. Nicolai, F. Renou, Mixed iota and kappa carrageenan gels in the presence of both calcium and potassium ions, Carbohydr. Polym. 223 (2019) 115107, https://doi.org/10.1016/j.carbpol.2019.115107.
[78] X. Gan, C. Li, J. Sun, X. Zhang, M. Zhou, Y. Deng, A. Xiao, GelMA/κ-carrageenan double-network hydrogels with superior mechanics and biocompatibility, RSC Adv. 13 (2023) 1558–1566, https://doi.org/10.1039/d2ra06101e.
[79] Z. Mohammadpour, M. Kharaziha, A. Zarrabi, 3D-Printing of silk nanofibrils reinforced alginate for soft tissue engineering, Pharmaceutics 15 (2023) 763, https://doi.org/10.3390/pharmaceutics15030763.

[80] X. Zhang, R. Zhang, S. Wu, Y. Sun, H. Yang, B. Lin, Physically and chemically dual-crosslinked hydrogels with superior mechanical properties and self-healing behavior, New J. Chem. 44 (2020) 9903–9911, https://doi.org/10.1039/d0nj00348d.

[81] Y. Huang, G. Sun, L. Lyu, Y. Li, D. Li, Q. Fan, J. Yao, J. Shao, Dityrosine-inspired photocrosslinking technique for 3D printing of silk fibroin-based composite hydrogel scaffolds, Soft Matter 18 (2022) 3705–3712, https://doi.org/10.1039/d1sm01817e.

[82] X. Mu, J.S.K. Yuan, J. Choi, Y. Zhang, P. Cebe, X. Jiang, Y.S. Zhang, D.L. Kaplan, Conformation-driven strategy for resilient and functional protein materials, Proc. Natl. Acad. Sci. U.S.A. 119 (2022) e2115523119, https://doi.org/10.1073/pnas.2115523119.

[83] C. Li, G. Guan, R. Reif, Z. Huang, R.K. Wang, Determining elastic properties of skin by measuring surface waves from an impulse mechanical stimulus using phase-sensitive optical coherence tomography, J. R. Soc. Interface 9 (2012) 831–841, https://doi.org/10.1098/rsif.2011.0583.

[84] F. Xu, T. Wen, T.J. Lu, K.A. Seffen, Skin biothermomechanics for medical treatments, J. Mech. Behav. Biomed. Mater. 1 (2008) 172–187, https://doi.org/10.1016/j.jmbbm.2007.09.001.

[85] A.C. Laly, K. Sliogeryte, O.J. Pundel, R. Ross, M.C. Keeling, D. Avisetti, A. Waseem, N. Gavara, J.T. Connelly, The keratin network of intermediate filaments regulates keratinocyte rigidity sensing and nuclear mechanotransduction, Sci. Adv. 7 (2021) eabd6187, https://doi.org/10.1126/sciadv.abd6187.

[86] P. Gupta, G. Hari Narayana, S N, U. Kasiviswanathan, T. Agarwal, K. Senthilguru, D. Mukhopadhyay, K. Pal, S. Giri, T.K. Maiti, I. Banerjee, Substrate stiffness does affect the fate of human keratinocytes, RSC Adv. 6 (2016) 3539–3551, https://doi.org/10.1039/c5ra19947f.

[87] R. Souron, F. Bordat, A. Farabet, A. Belli, L. Feasson, A. Nordez, T. Lapole, Sex differences in active tibialis anterior stiffness evaluated using supersonic shear imaging, J. Biomech. 49 (2016) 3534–3537, https://doi.org/10.1016/j.jbiomech.2016.08.008.

[88] J. Matalia, M. Francis, P. Gogri, P. Panmand, H. Matalia, A.S. Roy, Correlation of corneal biomechanical stiffness with refractive error and ocular biometry in a pediatric population, Cornea 36 (2017) 1221–1226, https://doi.org/10.1097/ico.0000000000001290.

[89] H. Lopez Hernandez, J.W. Souza, E.A. Appel, A quantitative description for designing the extrudability of shear-thinning physical hydrogels, Macromol. Biosci. 21 (2021) 2000295, https://doi.org/10.1002/mabi.202000295.

[90] M.M. Mrokowska, A. Krztoń-Maziopa, Viscoelastic and shear-thinning effects of aqueous exopolymer solution on disk and sphere settling, Sci. Rep. 9 (2019) 7897, https://doi.org/10.1038/s41598-019-44233-z.

[91] M.E. Cooke, D.H. Rosenzweig, The rheology of direct and suspended extrusion bioprinting, APL Bioeng. 5 (2021) 11502, https://doi.org/10.1063/5.0031475.

[92] Y. Wu, A. Wenger, H. Golzar, X. Shirley, Tang, 3D bioprinting of bicellular liver lobule-mimetic structures via microextrusion of cellulose nanocrystal-incorporated shear-thinning bioink, Sci. Rep. 10 (2020) 20648, https://doi.org/10.1038/s41598-020-77146-3.

[93] Y. Chen, X. Xiong, X. Liu, R. Cui, C. Wang, G. Zhao, W. Zhi, M. Lu, K. Duan, J. Weng, S. Qu, J. Ge, 3D Bioprinting of shear-thinning hybrid bioinks with excellent bioactivity derived from gellan/alginate and thixotropic magnesium phosphate-based gels, J. Mater. Chem. B 8 (2020) 5500–5514, https://doi.org/10.1039/d0tb00060d.

[94] M.E. Cooke, D.H. Rosenzweig, The rheology of direct and suspended extrusion bioprinting, APL Bioeng. 5 (2021) 011502, https://doi.org/10.1063/5.0031475.

[95] J.A. Lewis, Direct ink writing of 3D functional materials, Adv. Funct. Mater. 16 (2006) 2193–2204, https://doi.org/10.1002/adfm.200600434.

[96] W. Liu, M.A. Heinrich, Y. Zhou, A. Akpek, N. Hu, X. Liu, X. Guan, Z. Zhong, X. Jin, A. Khademhosseini, Y.S. Zhang, Extrusion bioprinting of shear-thinning gelatin methacryloyl bioinks, Adv. Healthcare Mater. 6 (2017) 1601451, https://doi.org/10.1002/adhm.201601451.

[97] M.E. Cooke, D.H. Rosenzweig, The rheology of direct and suspended extrusion bioprinting, APL Bioeng. 5 (2021) 011502, https://doi.org/10.1063/5.0031475.

[98] A. Blaeser, D. Filipa Duarte Campos, U. Puster, W. Richtering, M.M. Stevens, H. Fischer, A. Blaeser, D.F. Duarte Campos, U. Puster, H. Fischer, W. Richtering, M.M. Stevens, Controlling shear stress in 3D bioprinting is a key factor to balance printing resolution and stem cell integrity, Adv. Healthcare Mater. 5 (2016) 326–333, https://doi.org/10.1002/adhm.201500677.

[99] S. Iglauer, Y. Wu, P. Shuler, Y. Tang, W.A. Goddard, Dilute iota- and kappa-carrageenan solutions with high viscosities in high salinity brines, J. Pet. Sci. Eng. 75 (2011) 304–311, https://doi.org/10.1016/j.petrol.2010.11.025.

[100] D.A. Rees, Structure, conformation, and mechanism in the formation of polysaccharide gels and networks, Adv. Carbohydr. Chem. Biochem. 24 (1969) 267–332, https://doi.org/10.1016/s0065-2318(08)60352-2.

[101] N. Paxton, W. Smolan, T. Böck, F. Melchels, J. Groll, T. Jungst, Proposal to assess printability of bioinks for extrusion-based bioprinting and evaluation of rheological properties governing bioprintability, Biofabrication 9 (2017) 044107, https://doi.org/10.1088/1758-5090/aa8dd8.

[102] S. Joas, G.E.M. Tovar, O. Celik, C. Bonten, A. Southan, Extrusion-based 3D printing of poly(ethylene glycol) diacrylate hydrogels containing positively and negatively charged groups, Gels 4 (2018) (2018) 69, https://doi.org/10.3390/gels4030069.

[103] N.E.A. El-Naggar, M.H. Hussein, S.A. Shaaban-Dessuuki, S.R. Dalal, Production, extraction and characterization of Chlorella vulgaris soluble polysaccharides and their applications in AgNPs biosynthesis and biostimulation of plant growth, Sci. Rep. 10 (2020), https://doi.org/10.1038/s41598-020-59945-w.

[104] Y.-C. Yeh, C.B. Highley, L. Ouyang, J.A. Burdick, 3D printing of photocurable poly (glycerol sebacate) elastomers, Biofabrication 8 (2016) 045004, https://doi.org/10.1088/1758-5090/8/4/045004.

[105] J. Jia, D.J. Richards, S. Pollard, Y. Tan, J. Rodriguez, R.P. Visconti, T.C. Trusk, M. J. Yost, H. Yao, R.R. Markwald, Y. Mei, Engineering alginate as bioink for bioprinting, Acta Biomater. 10 (2014) 4323–4331, https://doi.org/10.1016/j.actbio.2014.06.034.

[106] S. Das, F. Pati, S. Chameettachal, S. Pahwa, A.R. Ray, S. Dhara, S. Ghosh, Enhanced redifferentiation of chondrocytes on microperiodic silk/gelatin scaffolds: toward tailor-made tissue engineering, Biomacromolecules 14 (2013) 311–321, https://doi.org/10.1021/bm301193t.

[107] L. Ouyang, J.P.K. Armstrong, Y. Lin, J.P. Wojciechowski, C. Lee-Reeves, D. Hachim, K. Zhou, J.A. Burdick, M.M. Stevens, Expanding and optimizing 3D bioprinting capabilities using complementary network bioinks, Sci. Adv. 6 (2020) 5529–5547, https://doi.org/10.1126/sciadv.abc5529.

[108] G. Basara, X. Yue, P. Zorlutuna, Dual crosslinked gelatin methacryloyl hydrogels for photolithography and 3D printing, Gels 5 (2019) 34, https://doi.org/10.3390/gels5030034.

[109] S. Das, F. Pati, Y.J. Choi, G. Rijal, J.H. Shim, S.W. Kim, A.R. Ray, D.W. Cho, S. Ghosh, Bioprintable, cell-laden silk fibroin-gelatin hydrogel supporting multilineage differentiation of stem cells for fabrication of three-dimensional tissue constructs, Acta Biomater. 11 (2015) 233–246, https://doi.org/10.1016/j.actbio.2014.09.023.

[110] S. Chawla, S. Midha, A. Sharma, S. Ghosh, Silk-based bioinks for 3D bioprinting, Adv. Healthcare Mater. 7 (2018) e1701204, https://doi.org/10.1002/adhm.201701204.

[111] M. Bonany, L. del-Mazo-Barbara, M. Espanol, M.P. Ginebra, Microsphere incorporation as a strategy to tune the biological performance of bioinks, J. Tissue Eng. 13 (2022) 20417314221119895, https://doi.org/10.1177/20417314221119895.

[112] B. Frohm, J.E. Denizio, D.S.M. Lee, L. Gentile, U. Olsson, J. Malm, K.S. Åkerfeldt, S. Linse, A peptide from human semenogelin I self-assembles into a pH-responsive hydrogel, Soft Matter 11 (2015) 414–421, https://doi.org/10.1039/c4sm01793e.

[113] J.H.Y. Chung, S. Naficy, Z. Yue, R. Kapsa, A. Quigley, S.E. Moulton, G.G. Wallace, Bio-ink properties and printability for extrusion printing living cells, Biomater. Sci. 1 (2013) 763–773, https://doi.org/10.1039/c3bm00012e.

[114] A. Kostenko, S. Swioklo, C.J. Connon, Effect of calcium sulphate pre-crosslinking on rheological parameters of alginate based bio-Inks and on human corneal stromal fibroblast survival in 3D bio-printed constructs, Front. Mech. Eng. 8 (2022) 867685, https://doi.org/10.3389/fmech.2022.867685.

[115] K. Ioannidis, R.I. Danalatos, S. Champeris Tsaniras, K. Kaplani, G. Lokka, A. Kanellou, D.J. Papachristou, G. Bokias, Z. Lygerou, S. Taraviras, A custom ultra-low-cost 3D bioprinter supports cell growth and differentiation, Front. Bioeng. Biotechnol. 8 (2020) 580889, https://doi.org/10.3389/fbioe.2020.580889.

[116] L. Ouyang, R. Yao, Y. Zhao, W. Sun, Effect of bioink properties on printability and cell viability for 3D bioplotting of embryonic stem cells, Biofabrication 8 (2016) 035020, https://doi.org/10.1088/1758-5090/8/3/035020.

[117] A. Schwab, R. Levato, M. D'Este, S. Piluso, D. Eglin, J. Malda, Printability and shape fidelity of bioinks in 3D bioprinting, Chem. Rev. 120 (2020) 11028–11055, https://doi.org/10.1021/acs.chemrev.0c00084.

[118] H. Jongprasitkul, S. Turunen, V.S. Parihar, M. Kellomäki, Two-step crosslinking to enhance the printability of methacrylated gellan gum biomaterial ink for extrusion-based 3D bioprinting, Bioprinting 25 (2022) e00185, https://doi.org/10.1016/j.bprint.2021.e00185.

[119] S. Kyle, Z.M. Jessop, A. Al-Sabah, I.S. Whitaker, 'Printability'' of candidate biomaterials for extrusion based 3D printing: state-of-the-art, Adv. Healthcare Mater. 6 (2017) 1700264, https://doi.org/10.1002/adhm.201700264.

[120] S. Ramasamy, P. Davoodi, S. Vijayavenkataraman, J.H. Teoh, A. M. Thamizhchelvan, K.S. Robinson, B. Wu, J.Y.H. Fuh, T. DiColandrea, H. Zhao, E.B. Lane, C.H. Wang, Optimized construction of a full thickness human skin equivalent using 3D bioprinting and a PCL/collagen dermal scaffold, Bioprinting 21 (2021) e00123, https://doi.org/10.1016/j.bprint.2020.e00123.

[121] T.Y. Park, Y.J. Yang, D.-H. Ha, D.-W. Cho, H.J. Cha, Marine-derived natural polymer-based bioprinting ink for biocompatible, durable, and controllable 3D constructs, Biofabrication 11 (2019) 035001, https://doi.org/10.1088/1758-5090/ab0c6f.

[122] Y.P. Singh, A. Bandyopadhyay, B.B. Mandal, 3D Bioprinting using cross-linker-free silk-gelatin bioink for cartilage tissue engineering, ACS Appl. Mater. Interfaces 11 (2019) 33684–33696, https://doi.org/10.1021/acsami.9b11644.

[123] I. Bružauskaitė, D. Bironaitė, E. Bagdonas, E. Bernotienė, Scaffolds and cells for tissue regeneration: different scaffold pore sizes—different cell effects, Cytotechnology 68 (2016) 355, https://doi.org/10.1007/S10616-015-9895-4.

[124] S.J. Lee, J.S. Choi, K.S. Park, G. Khang, Y.M. Lee, H.B. Lee, Response of MG63 osteoblast-like cells onto polycarbonate membrane surfaces with different micropore sizes, Biomaterials 25 (2004) 4699–4707, https://doi.org/10.1016/j.biomaterials.2003.11.034.

[125] Y. Ma, Y. You, L. Cao, B. Liang, B. Tian, J. Dong, H. Lin, Improved osteogenesis by mineralization combined with double-crosslinked hydrogel coating for proliferation and differentiation of mesenchymal stem cells, Front. Bioeng. Biotechnol. 9 (2021) 706423, https://doi.org/10.3389/fbioe.2021.706423.

[126] H. Zhang, D. Xu, Y. Zhang, M. Li, Renjie Chai, R. Chai, Silk fibroin hydrogels for biomedical applications, Smart Med 1 (2022) e20220011, https://doi.org/10.1002/smmd.20220011.

[127] C. Holland, K. Numata, J. Rnjak-Kovacina, F.P. Seib, The biomedical use of silk: past, present, future, Adv. Healthcare Mater. 8 (2019) 1800465, https://doi.org/10.1002/adhm.201800465.
[128] S. Wang, Y. Xiong, J. Chen, A. Ghanem, Y. Wang, J. Yang, B. Sun, Three dimensional printing bilayer membrane scaffold promotes wound healing, Front. Bioeng. Biotechnol. 7 (2019) 348, https://doi.org/10.3389/fbioe.2019.00348.
[129] Z. Wu, X. Su, Y. Xu, B. Kong, W. Sun, S. Mi, Bioprinting three-dimensional cell-laden tissue constructs with controllable degradation, Sci. Rep. 6 (2016) 24474, https://doi.org/10.1038/srep24474.
[130] F. Pati, J. Jang, D.H. Ha, S. Won Kim, J.W. Rhie, J.H. Shim, D.H. Kim, D.W. Cho, Printing three-dimensional tissue analogues with decellularized extracellular matrix bioink, Nat. Commun. 5 (2014) 3935, https://doi.org/10.1038/ncomms4935.
[131] B. Derby, Printing and prototyping of tissues and scaffolds, Science 338 (2012) 921–926, https://doi.org/10.1126/science.1226340.
[132] J. Zhang, H. Eyisoylu, X.H. Qin, M. Rubert, R. Müller, 3D bioprinting of graphene oxide-incorporated cell-laden bone mimicking scaffolds for promoting scaffold fidelity, osteogenic differentiation and mineralization, Acta Biomater. 121 (2021) 637–652, https://doi.org/10.1016/j.actbio.2020.12.026.
[133] S. Boularaoui, G. Al Hussein, K.A. Khan, N. Christoforou, C. Stefanini, An overview of extrusion-based bioprinting with a focus on induced shear stress and its effect on cell viability, Bioprinting 20 (2020) e00093, https://doi.org/10.1016/j.bprint.2020.e00093.
[134] J. Adhikari, A. Roy, A. Das, M. Ghosh, S. Thomas, A. Sinha, J. Kim, P. Saha, J. Adhikari, A. Das, A. Sinha, A. Roy, M. Ghosh, S. Thomas, J. Kim, P. Saha, Effects of processing parameters of 3D bioprinting on the cellular activity of bioinks, Macromol. Biosci. 21 (2021) 2000179, https://doi.org/10.1002/mabi.202000179.
[135] O. Ajiteru, K.Y. Choi, T.H. Lim, D.Y. Kim, H. Hong, Y.J. Lee, J.S. Lee, H. Lee, Y. J. Suh, M.T. Sultan, O.J. Lee, S.H. Kim, C.H. Park, A digital light processing 3D printed magnetic bioreactor system using silk magnetic bioink, Biofabrication 13 (2021) 034102, https://doi.org/10.1088/1758-5090/abfaee.
[136] S. Abbasi-Ravasjani, H. Seddiqi, A. Moghaddaszadeh, M.E. Ghiasvand, J. Jin, E. Oliaei, R.G. Bacabac, J. Klein-Nulend, Sulfated carboxymethyl cellulose and carboxymethyl κ-carrageenan immobilization on 3D-printed poly-ε-caprolactone scaffolds differentially promote pre-osteoblast proliferation and osteogenic activity, Front. Bioeng. Biotechnol. 10 (2022) 957263, https://doi.org/10.3389/fbioe.2022.957263/bibtex.
[137] M. Levy-Mishali, J. Zoldan, S. Levenberg, Effect of scaffold stiffness on myoblast differentiation, Tissue Eng. 15 (2009) 935–944, https://doi.org/10.1089/ten.tea.2008.0111.
[138] R. Sunyer, A.J. Jin, R. Nossal, D.L. Sackett, Fabrication of hydrogels with steep stiffness gradients for studying cell mechanical response, PLoS One 7 (2012) e46107, https://doi.org/10.1371/journal.pone.0046107.
[139] Y. Wang, G. Wang, X. Luo, J. Qiu, C. Tang, Substrate stiffness regulates the proliferation, migration, and differentiation of epidermal cells, Burns 38 (2012) 414–420, https://doi.org/10.1016/j.burns.2011.09.002.
[140] P.A. Janmey, R.T. Miller, Mechanisms of mechanical signaling in development and disease, J. Cell Sci. 124 (2011) 9–18, https://doi.org/10.1242/jcs.071001.
[141] D. Sicard, A.J. Haak, K.M. Choi, A.R. Craig, L.E. Fredenburgh, D.J. Tschumperlin, Aging and anatomical variations in lung tissue stiffness, Am. J. Physiol. Lung Cell Mol. Physiol. 314 (2018) L946–L955, https://doi.org/10.1152/ajplung.00415.2017.
[142] C. Qin, J. Ma, L. Chen, H. Ma, H. Zhuang, M. Zhang, Z. Huan, J. Chang, N. Ma, C. Wu, 3D bioprinting of multicellular scaffolds for osteochondral regeneration, Mater. Today 49 (2021) 68–84, https://doi.org/10.1016/j.mattod.2021.04.016.
[143] D. Baruffaldi, G. Palmara, C. Pirri, F. Frascella, 3D cell culture: Recent development in materials with tunable stiffness, ACS Appl. Bio Mater. 4 (2021) 2233–2250, https://doi.org/10.1021/acsabm.0c01472.
[144] V. Palmieri, F. Sciandra, M. Bozzi, M. De Spirito, M. Papi, 3D graphene scaffolds for skeletal muscle regeneration: future perspectives, Front. Bioeng. Biotechnol. 8 (2020) 383, https://doi.org/10.3389/fbioe.2020.00383.
[145] Y.P. Singh, N. Bhardwaj, B.B. Mandal, Potential of agarose/silk fibroin blended hydrogel for in vitro cartilage tissue engineering, ACS Appl. Mater. Interfaces 8 (2016) 21236–21249, https://doi.org/10.1021/acsami.6b08285.
[146] L. Yildirimer, N.T.K. Thanh, A.M. Seifalian, Skin regeneration scaffolds: a multimodal bottom-up approach, Trends Biotechnol. 30 (2012) 638–648, https://doi.org/10.1016/j.tibtech.2012.08.004.
[147] G. Yang, Z. Xiao, X. Ren, H. Long, H. Qian, K. Ma, Y. Guo, Enzymatically crosslinked gelatin hydrogel promotes the proliferation of adipose tissue-derived stromal cells, PeerJ 4 (2016) e2497, https://doi.org/10.7717/peerj.2497.
[148] J. Ye, G. Yang, J. Zhang, Z. Xiao, L. He, H. Zhang, Q. Liu, Preparation and characterization of gelatin-polysaccharide composite hydrogels for tissue engineering, PeerJ 9 (2021) e11022, https://doi.org/10.7717/peerj.11022.
[149] M. Li, M. Ogiso, N. Minoura, Enzymatic degradation behavior of porous silk fibroin sheets, Biomaterials 24 (2003) 357–365, https://doi.org/10.1016/S0142-9612(02)00326-5.
[150] N. Bhardwaj, Y.P. Singh, D. Devi, R. Kandimalla, J. Kotoky, B.B. Mandal, Potential of silk fibroin/chondrocyte constructs of muga silkworm Antheraea assamensis for cartilage tissue engineering, J. Mater. Chem. B 4 (2016) 3670–3684, https://doi.org/10.1039/c6tb00717a.
[151] R.G. Patel, A. Purwada, L. Cerchietti, G. Inghirami, A. Melnick, A.K. Gaharwar, A. Singh, Microscale bioadhesive hydrogel arrays for cell engineering applications, Cell. Mol. Bioeng. 7 (2014) 394–408, https://doi.org/10.1007/s12195-014-0353-8.
[152] F.F. Schmidt, S. Nowakowski, P.J. Kluger, Improvement of a three-layered in vitro skin model for topical application of irritating substances, Front. Bioeng. Biotechnol. 8 (2020) 388, https://doi.org/10.3389/fbioe.2020.00388.
[153] E. Hofmann, A. Schwarz, J. Fink, L.-P. Kamolz, P. Kotzbeck, Modelling the complexity of human skin in vitro, Biomedicines 11 (2023) 794, https://doi.org/10.3390/biomedicines11030794.
[154] S.L. Flores, F.B.A. Descallar, S. Matsukawa, R.G. Bacabac, Dynamic rheological properties of mixed carrageenan gels under large strains, J. Biorheol. 31 (2017) 35–39, https://doi.org/10.17106/jbr.31.35.
[155] T. Masuko, A. Minami, N. Iwasaki, T. Majima, S.I. Nishimura, Y.C. Lee, Carbohydrate analysis by a phenol–sulfuric acid method in microplate format, Anal. Biochem. 339 (2005) 69–72, https://doi.org/10.1016/j.ab.2004.12.001.
[156] F. Yue, J. Zhang, J. Xu, T. Niu, X. Lü, M. Liu, Effects of monosaccharide composition on quantitative analysis of total sugar content by phenol-sulfuric acid method, Front. Nutr. 9 (2022) 963318, https://doi.org/10.3389/fnut.2022.963318.